Tel-Aviv University
Raymond and Beverly Sackler
Faculty of Exact Sciences

Analysis and Quality Tests of the ATLAS Muon Endcap Trigger Chambers.

Thesis submitted toward the M.Sc. Degree
in Tel-Aviv University
The Department of Physics and Astronomy
By

Jonathan Ginzburg

The research work for this thesis was carried out in the Experimental High Energy Physics group of Tel-Aviv University under the supervision of Dr. Erez Etzion

January 2003

Abstract

The subject of this thesis is the design and operation of the data acquisition system, which serves to analyze and to test the performance of the Thin Gap Chambers (TGC) detector. The TGCs are detectors designed to detect the high transverse momentum muons in the endcaps of the ATLAS detector. The ATLAS Collaboration is building a general-purpose pp detector, which is design to exploit the full discovery potential of the High Energy proton-proton interaction in the Large Hadron Collider (LHC) currently built at CERN. The LHC will offer a large range of physics opportunities, among which the origin of mass at the electroweak scale. The short time response of the TGCs makes it an ideal trigger system for selecting interesting events in the highly packed environment of the LHC accelerator. Being part of the trigger system of the ATLAS experiment it is required that the TGCs will reach uniform high detection efficiency in a fast time response. The testbench build in Tel-Aviv University, uses muon from Cosmic Rays to test that performance.

Acknowledgements

I would like to thank Dr. Erez Etzion for giving me this unique opportunity to join the research program of the Tel Aviv HEP group.
I am deeply indebted to my friends and colleagues from the laboratory Meny Ben-Moshe, Jack Wasilewsky, Elad Tsur and Dr Yan Benhamu for their daily professional and personal support. Without their company and help I would have been lost. I very much appreciate the support given to me by Dr. Juliana Cohen and Dr.Gideon Bella. I wish to express my thanks to Yoram Granitzky and Eduardo Warszawski from the Technion for their help with the hardware and software design. I cannot possibly name all the people who made my work easier and I thank them all from the bottom of my heart.
I dedicate this thesis to my parents. Without them I would never have accomplished this work.

1. Introduction 7
2. The LHC physics 8
3. The ATLAS detector 10
3.1. The detector structure 11
3.2. Trigger and data-acquisition system 13
4. Instrumentation of the Muon Spectrometer 15
4.1. Muon chamber layout 15
4.2. Design of TGC chambers 18
4.3. **Mechanical structure of TGC units** 20
4.4. Principle of muon triggering with TGCs 21
4.5. The TGC readout 22
5. TGCs efficiency test 23
5.1. General description 23
5.2. Cosmic ray telescope 24
5.3. Trigger signal 25
5.4. Precision chambers 27
5.5. The gas system 27
5.6. The readout scheme 28
5.7. The online readout software 32
6. Analysis 33
6.1. Study of the test-bench timing 34
6.1.1. Scintillator time calculation 34
6.2. Muon reconstruction 37
6.2.1. Selection of one-muon candidates 37
6.2.2. Position reconstruction 40
6.2.3. Trajectory calculation 43
6.2.4. Systematic error uncertainties 44
7. Results 48
7.1. Efficiency mapping of tested chambers 48
7.2. Alignment procedure 51
7.3. Determination of the inefficient areas 55
7.4. Potential problems 57
7.5. High voltage dependence 58
8. Summary 59
Appendix 61
Appendix I: **Binary online output file** 61
Appendix II: **The multiple scattering** 64

Table of Figures

Fig. 1: Sensitivity for the discovery of a SM Higgs boson in the LHC experiments as a function of the Higgs mass. The signal significances, assuming an integrated luminosity of 100 fb^{-1} , is plotted in terms of standard deviations, for individual channels (different symbols as defined in the figure), as well as for the combination of all channels (full line) (see ref.). 9
Fig. 2: Schematic view of Atlas detector. 11
Fig. 3: Block diagram of the Trigger/DAQ system 13
Fig. 4: Three-dimensional view of the muon spectrometer instrumentation indicating the areas covered by the four chamber technologies. 15
Fig. 5 : Muon chambers geometry relatively to the interaction point. 17
Fig. 6: Resolution of the muon transverse momentum, $\Delta P_T / P_T$, as a function of η , as expected from the measurements provided by the muon spectrometer. 17
Fig. 7: Schematic view of a thin gap chamber 18
Fig. 8: View of a T8 TGC chamber from above. The upper yellow area depicts the geometry of the strips. The lower area, under the strips depicts the mesh of wires, perpendicular to the strips. The supports of the wires are also shown. 19
Fig. 9: A side view of one ATLAS quadrant. In black the muon trajectories. Both the barrel and the end cap muon trigger principle is depicted. The trajectories generated in the IP are shown for positive and negative muons. 22
Fig. 10: The testbench schematic structure 25
Fig. 11: The emitance spectrum of the scintillator material. 25
Fig. 12 : The working spectrum of the PMT. 26
Fig. 13:The structure of one scintillator detector. 26
Fig. 14 Picture of scintillator slabs with their lightguides. One of them is already wrapped with black plastic sheet and two phototubes are seen as well. 27
Fig. 15: The structure of the precision chamber. 27
Fig. 16: Schematic diagram of connections between the scintillators. 29
Fig. 17:The electronic connection of the precision chamber. 30
Fig. 18: The layout of the readout system. 31
Fig. 19: The Data Acquisition flow. 32
Fig. 20: Detecting the generated photons in the scintillator. 34
Fig. 21 : The time difference between left and right sides of the scintillator detector. 35
Fig. 22: The Top scintillator time minus Bottom one. 36
Fig. 23: The time difference between pulses originally generated with 40 ns gap between them. 37
Fig. 24: The distribution of the number of strips per event. 38
Fig 25: A logarithmic distribution of the ratio of P_{SUB} over P_{TOT} 39
Fig 26: The average distribution of the voltage in the PRC strips, around the strip in the cluster with the maximal voltage, denoted as zero in the figure. 41
Fig 27: The distribution of the difference $\overline{x}_W$ - $\overline{x}_G$ 42
Fig. 28: The equation for the line connecting the two coordinates. 43
Fig. 29: Trajectory calculation. In yellow the top and bottom precision chambers, in red a TGC plane. 44
Fig. 30: The distribution of the error in position difference Δx 45

Fig. 31: Top histogram is the distribution of the distance between the measured hits in the TGC, placed in the testbench center, and the extrapolated ones. The bottom plot contains nine histograms. Each of which represents the error distribution for a certain layer in the testbench. 46
Fig 32: The graph of the widths in distributions in bottom plot of Fig. 31 as a function of the relative position in the testbench. 47
Fig 33: The hits expected in the TGC as extrapolated from the PRC information. 48
Fig. 34: The actual muons hits in the TGC. 49
Fig. 35: The efficiency map of a doublet U08F2I-521.0. Figures A, B presents the wires (left) and Strips (right) of the bottom chamber, where C, D respectively present the wires and the strips of the top chamber. The colors stand for the efficiency in the measured surfaces. Efficiency >95% is white, 90-95% is yellow, 85-90% is green, where at the other side of the scale efficiency below50% is plotted in black. 50
Fig.36: The profile of the single support in a resolution of one mm. 52
Fig. 37: An example of the unaligned chamber (strips) efficiency plot. 53
Fig. 38: The efficiency histograms (wires and strips of its two chambers) of the unit U08F3I-713.4, with bin size of one mm^2 54
Fig. 39: The efficiency histogram of the chamber in Fig 36 here after the alignment procedure 55
Fig. 40: Top – efficiency plot of one chamber's strip; Bottom - the detected inefficient regions in the above chamber. 56
Fig. 41: The example of the unit U08B3I-624.1 with some imperfections 57
Fig. 42: The efficiency map of the one chamber operating at the nominal high voltage of the 2.9 kV. 58
Fig. 43: The efficiency map of the same chamber (Fig. 42) operating at 3kV. 58
Fig. 44: Inefficient regions distribution, as detailed in the text. 60
Fig. 45: Shows a typical output file. 62

1. Introduction

The Large Hadron Collider (LHC) is a new proton-proton collider under construction at European Center for Nuclear Research (CERN) to be installed in an existing tunnel, with previously housed the Large Electron Positron (LEP) tunnel at the. It will collide 7 TeV protons and the design luminosity is 10^{34} cm^{-2} s^{-1}.

About 30 fb^{-1} are expected to be collected during the first three years (2007-2009), when the machine will run at low luminosity (10^{33} cm^{-2} s^{-1}), while about 100 fb^{-1} per year will be collected when running at design luminosity. Four experiments have been approved and are under construction. Two experiments, ATLAS and CMS will study pp collisions. The Alice experiment is designed to study heavy ion collisions, when heavy ion beams will be injected into the LHC. The fourth experiment, LHCB, will operate with only one proton beam hitting stationary targets, with the goal to measuring beauty production.

The Tel-Aviv University High Energy Group is collaborating in one of the two pp experiments, the ATLAS experiment. This experiment has a great discovery potential for new physics. For example a Standard Model Higgs boson can be discovered over the full range of kinematically allowed masses.

The Thin Gap Chambers (TGCs) are detectors designed to detect the high transverse momentum muons in the endcaps of the ATLAS detector. The short response time of the TGCs makes it an ideal trigger system for selecting interesting events in the highly packed environment of the LHC accelerator. The TGCs are designed and built in Weizmann Institute in Israel as well as in KEK in Japan and in China. There are three test-benches to check the performance of the TGC modules, two in Israel, one in the Technion and one in the Tel-Aviv University, and a third in Kobe University in Japan. The purpose of these tests is to provide a detailed map of detection efficiency.
A cosmic ray telescope was built in Tel-Aviv University for these tests. The Testbench can test up to 7 TGC units in parallel. Accumulating events for a period of one week will provide a full mapping of the efficiency of each detector in the required resolution.

The subject of this thesis is the design and operation of the data acquisition system, which serves to analyze and to test the performance of the TGC detector, before they are installed in the ATLAS experiment.

In Chapter 2 a theoretical background of LHC and the ATLAS experiment are briefly summarized. Chapter 3 describes the ATLAS detector and the trigger system. Chapter 4 presents the TGC detectors in the Muon Spectrometer and their role in the triggering scheme of the ATLAS experiment. We are using muons from cosmic rays to test the chambers performance. Chapter 5 describes the experimental setup: the detectors that are used in the testbench and the readout system. The data analysis and the results are presented in Chapters 6 and 7.

2. The LHC physics

The Standard Model (SM)[1] provides a very successful description of interactions of the constituents of matter down to the smallest distances (10^{-18} m) and up to highest energies (~200GeV) accessible to current experiments. It is based on quantum field theory in which interactions of spin ½ , point-like fermions are mediated by spin 1 gauge bosons.
The gauge theory part of the SM has been well tested, but there is no direct evidence either for or against the Higgs[2] mechanism for electroweak symmetry breaking. In the SM all masses are tied to the mass scale of the Higgs sector, however the model does not provide guidance for the Higgs mass. Present experimental results interpreted in term of the SM Higgs, point to the mass of the Higgs boson in the range 160 to 200 GeV. The experimental observation of one or several Higgs bosons will be fundamental for a better understanding of the mechanism of electroweak symmetry breaking.

In the SM, one doublet of scalar field is assumed for symmetry breaking, leading to the existence of one neutral scalar Higgs particles, H. In supersymmetric theories, the Higgs sector is extended to contain at least two doublets of scalar fields.
In the minimal version, the so-called minimal supersymmetric SM (MSSM) model, there are five physical charged Higgs particles: CP even, h, H, one CP odd, A, and two charged $H^{\pm}$. Two parameters, which are generally chosen to be the mass of the A Higgs, m_A and tan(β), the ratio of the vacuum expectation values of the Higgs doublets, determine the structure of the Higgs sector at tree level.
The dominant production mechanism of a light Higgs boson at LHC energies is gluon-gluon fusion, which proceeds via heavy quark loops.

The overall sensitivity for the discovery of a SM Higgs boson is shown in *Fig. 1* for various decay channels, assuming an integrated luminosity of 100 fb^{-1}.
The decay channel $H \to ZZ^* \to 4l$ provides a rather clean signature in the mass range between ~120 GeV and $2m_Z$, above which the gold-plated channel with two real Z bosons in the final states opens up. Both electrons and muons are considered in the final state, thus yielding $eeee$, $ee\mu\mu$ and $\mu\mu\mu\mu$ event topologies. While production channels with W bosons are also of interest, they usually provide lower sensitivity.
If the SM Higgs boson were to be discovered at LHC, its mass, m_H, would be measured with a precision of 0.1% for $m_H < 400$ GeV and of 0.1-1% for $400 < m_H < 700$ GeV. The Higgs boson width can be determined for masses above 200 GeV using the $H \to ZZ^* \to 4l$ channel.

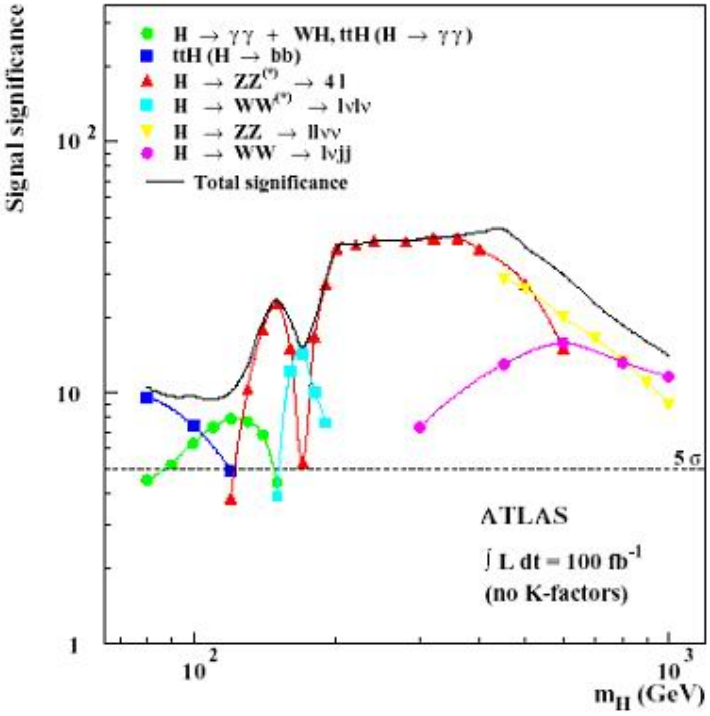

Fig. 1: Sensitivity for the discovery of a SM Higgs boson in the LHC experiments as a function of the Higgs mass. The signal significances, assuming an integrated luminosity of 100 fb^{-1}, is plotted in terms of standard deviations, for individual channels (different symbols as defined in the figure), as well as for the combination of all channels (full line) (see ref. [3]).

The capability of LHC experiments to detect MSSM Higgs bosons has been studied in depth over the last few years [4]. It is usually assumed that the supersymmetric particles are heavy enough, so that the decay of the Higgs bosons proceeds through channels involving the known particle spectra. In the MSSM, various decay modes accessible also in the case of the SM Higgs boson, are predicted such as $h \to \gamma\gamma$, $h \to b\bar{b}$, $H \to ZZ^* \to 4l$. In addition, some channels such as $H/A \to \tau\tau$ and $H/A \to \mu\mu$ are strongly enhanced if $\tan\beta$ happens to be large. Complete coverage of the region will be possible at LHC. Over a considerable fraction of the parameter space, at least two channels are accessible and/or more than one Higgs bosons can be observed. In most cases, the experiments will be capable of distinguishing between a SM and an MSSM Higgs boson.

If supersymmetry (SUSY) indeed exists at the electroweak scale, then the SUSY cross-section is dominated by gluinos and squarks production[5], and the cross-sections are expected to be large. Gluinos and squarks decay sequentially into the lightest supersymmetric particle (LSP) (which may decay further, if the supersymmetric quantum number, the R-parity is violated). These decay chains lead to a variety of signatures in the final state involving multiple jets, leptons, photons, heavy flavors, W and Z bosons, as well as missing energy. The combination of a large production cross-section and distinctive signatures makes it easy to separate SUSY from the SM background. Therefore, the main challenge will not be to discover SUSY, but to separate the many SUSY processes that occur and to measure the masses and other properties of the SUSY particles. In most cases, the backgrounds from other SUSY events dominate over the reducible SM backgrounds.

In summary, if a Higgs boson, with $m_H < 1$ TeV, exists, it will be discovered at LHC. The same is true of supersymmetric particles. The properties of the production and decay mechanisms define the required performance of the detector, presently at the construction stage.

3. The ATLAS detector

ATLAS is one of the general-purpose detectors designed by International Collaboration of 35 countries, to fully exploit the discovery potential of proton-proton collisions at center of mass energy of 14 TeV.

A broad spectrum of detailed physics simulations led to the overall detector concept. The basic design criteria of the detector include the following.

- Large acceptance in pseudorapidity $\eta = -\ln tg\frac{\Theta}{2}$, where Θ is the polar angle, with almost full azimuthal coverage everywhere.
- Efficient tracking with full event reconstruction at low luminosity and preserved capability to measure high transverse momentum, p_T, muons, to identify electrons, τ leptons and heavy flavors in the high luminosity environment.
- Very good electromagnetic calorimetry for electron and positron identification and measurements, complemented by a full coverage hadron calorimetry for accurate jets and missing transverse energy E_T^{miss} measurements.
- High precision Muon spectrometer for muon momentum measurements, down to p_T of 6 GeV even at the highest luminosity.
- Triggering system providing high efficiencies for most physics processes of interest at LHC.

3.1. The detector structure

The overall detector layout is shown in *Fig. 2*.
The detector is 44 m long 22m high and weighs 7000 tons.

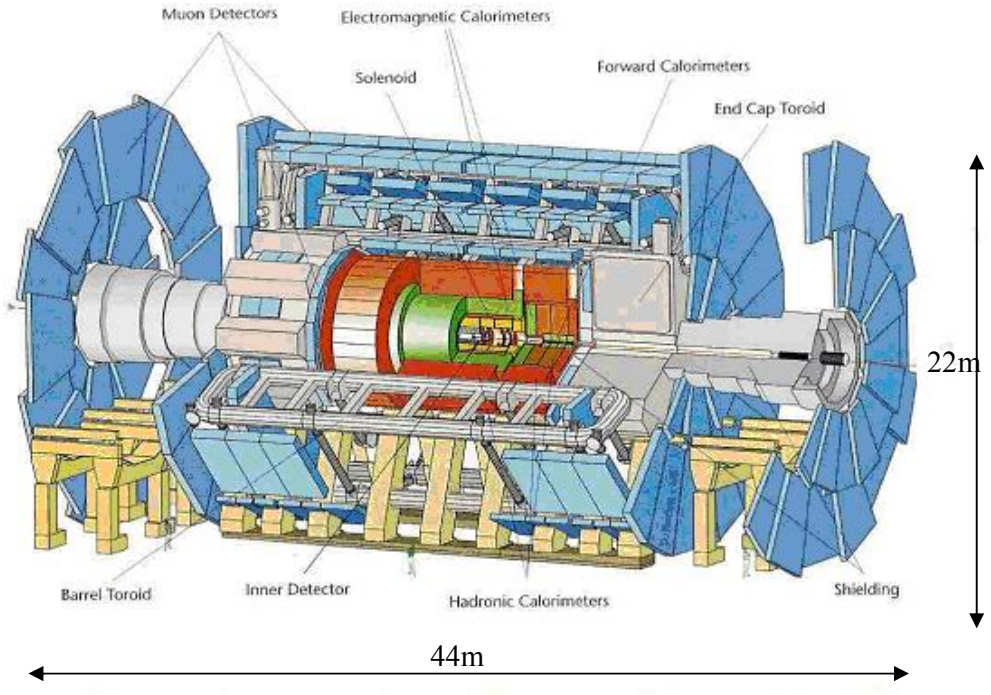

Fig. 2: Schematic view of Atlas detector.

The magnet configuration is based on an inner superconducting solenoid, surrounding the inner detector and the electromagnetic calorimeter, and large superconducting air-core toroids consisting of independent coils arranged around the hadronic calorimeter and the first station of muon chambers.

The inner detector is contained within a cylinder of length 6.80 m and radius 1.15 m. It operates in a solenoidal magnetic field of 2 T. A combination of discrete high-resolution pixel and strip detectors in the inner part and continuous straw-tube tracking detectors achieve the pattern recognition, momentum and vertex measurements, and enhanced electron identification.

Highly granular, Liquid Argon (LAr) electromagnetic sampling calorimetry, with lead (Pb) as absorber, with excellent performance in terms of energy and position resolutions, covers the pseudorapidity range $\eta < 3.2$. A plastic scintillator plates (tile) embedded in an iron (Fe) absorber, which is separated into one large barrel and two extended barrel cylinders on each side, provides the bulk of the hadronic calorimetry. The LAr calorimetry is contained in a cylinder with an outer radius of 2.25 m and extends to ±6.65 m along the beam axis. The outer radius of the tile calorimeter is 4.25 m and its length is 12.20 m.

In the end-caps the LAr technology is also used for the hadron calorimeter (Fe), sharing the cryostats with the electromagnetic end-cap calorimetry (Pb). The same cryostats also house the special LAr forward calorimeters (Fe), which extend the pseudorapidity coverage to $3.2 < \eta < 4.9$.

The calorimetry is surrounded by the muon spectrometer. The air-core toroid system, with a long barrel and two inserted end-cap magnets, generates a 0.6T magnetic field volume with a light and open structure. An excellent muon momentum resolution is achieved with three stations of high-precision tracking chambers and fast trigger chambers. The details of the muon chamber layout will be discussed in chapter 4.

3.2. Trigger and data-acquisition system

The task of the ATLAS trigger system is to reduce the input beam related rate of 10^9 Hz at the highest luminosity to about 100 Hz for permanent storage.

To handle this task the ATLAS trigger and data-acquisition (DAQ) system is based on three levels of online event selection. Each trigger level refines the decisions made at the previous level and, where necessary, applies additional selection criteria. While this requires an overall rejection factor of 10^7 against 'minimum-bias' events, excellent efficiency must be retained for the rare new physics processes, such as Higgs boson decays. *Fig. 3* shows a simplified functional view of the Trigger/DAQ system.

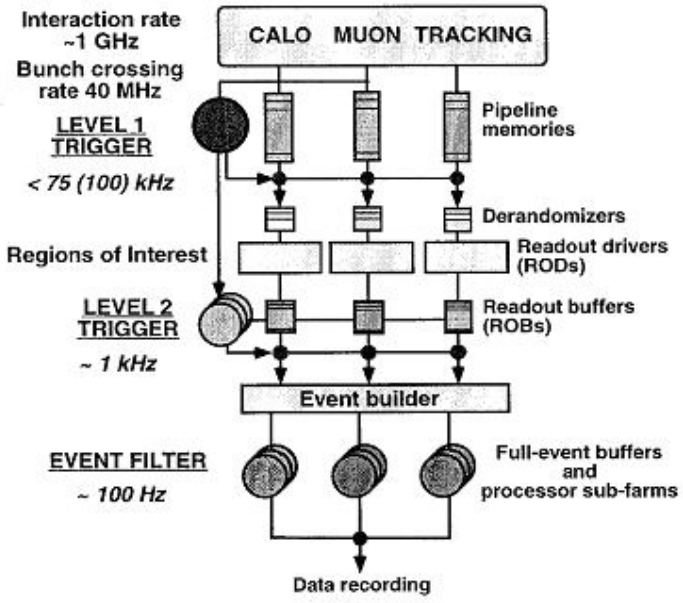

Fig. 3: Block diagram of the Trigger/DAQ system

The LVL1 trigger accepts data at the full LHC bunch-crossing rate of 40 MHz (every 25 ns). The time taken to form and distribute the LVL1 trigger decision (called latency) is about 2 μs, and the maximum output rate is limited to 100 kHz by the capabilities of the subdetector readout systems and the LVL2 trigger. During the LVL1 processing, the data from all parts of the ATLAS detector are held in pipeline memories. Requirements on the LVL1 trigger are that it must identify the bunch crossing containing the interaction of interest and introduce negligible dead time.

The LVL2 trigger reduces the rate from up to 100 kHz after LVL1 to about 1 kHz. The information from the LVL1 trigger system is used to identify the regions of the detector containing interesting features such as high- p_T, electrons, photons, jets and muons. The LVL2 trigger then has to access and process only a small fraction of the total detector data, with corresponding advantages in terms of the required processing power and data-movement capacity. The total LVL2 latency is variable, up to about 10 ms.

After an event is accepted by the LVL2 trigger, the full data are sent to the LVL3 processors via the event builder (EB). Complete event reconstruction is possible at LVL3, with decision times up to about 1 s. The LVL3 system must achieve a data-storage rate of 10-100 MB/s by reducing the event rate and/or the event size. For some triggers, for example Higgs boson candidates, the full event data will be recorded with an event size of about 1 MB, corresponding to a maximum event rate of about 100 Hz.

Only muon and calorimeter information is used in separate LVL1 processors to evaluate various trigger conditions. Inner detector information is not used at LVL1 because of the complexity of the events at high luminosity and because the rates can be reduced to acceptable levels without it. Full-precision information from the inner detector, as well as from the calorimeter and muon detectors, is however used at LVL2. The full data of each event accepted by LVL2 are assembled and transferred to a farm of processors that perform full-event analysis and make the LVL3 selection before permanent recording. The data-merging stage will be based on a high-speed switching network, interconnecting Data Acquisition (DAQ) memories and LVL3 processing units, supervised by data-flow manager components.

4. Instrumentation of the Muon Spectrometer

4.1. Muon chamber layout

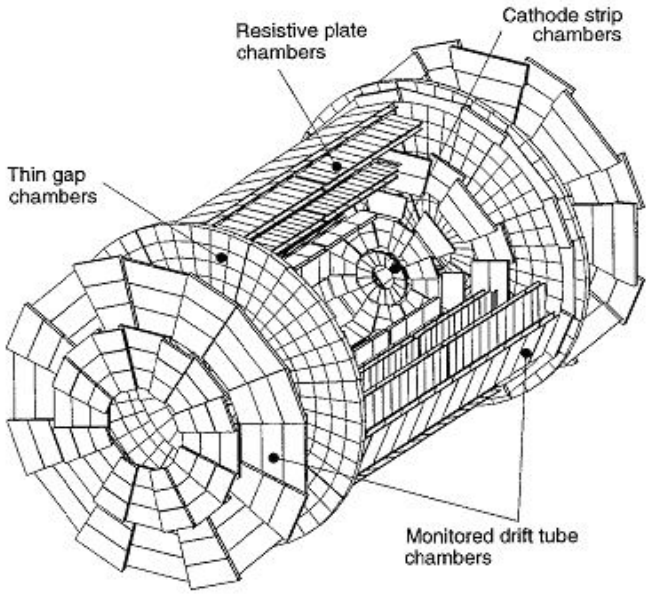

Fig. 4: Three-dimensional view of the muon spectrometer instrumentation indicating the areas covered by the four chamber technologies.

The overall layout of the muon chambers in the ATLAS detector is shown in *Fig. 4*, where the different regions with the four chamber technologies are indicated;

- the Monitor Drift Tube (MDT) chambers are used for precise tracking of muons;
- the Resistive Plate Chambers (RPC) are used for triggering in the barrel region of the ATLAS detector;
- the Thin Gap Chambers are used for triggering in the end-cap region of the ATLAS detector;
- the Cathode Strip Chambers are used for tracking muons in the end-cap region of the ATLAS detector in small angles.

The chambers are arranged such that particles from the interaction point traverse three stations of chambers. The position of these stations is optimized for essentially full coverage and good momentum resolution.

In the barrel region, the MDTs form three concentric cylinders (see *Fig. 5*), one located in front, one inside and one outside of the barrel air core toroid (BAT), at radii of 5, 7, 9 m from the interaction point respectively. This structure forms the three MDT stations in the barrel region. The second MDT station is sandwiched between two RPC trigger chamber layers. The last RPC layer is behind the last MDT station. These three RPC layers forms the RPC stations. The barrel stations cover the pseudorapidity range $|\eta|<1$.

In the end-cap, the three MDT stations are located such that one station is in front of the end-cap toroid (ECT), one is right behind, and the last one is placed about 7 m downstream from the second one. The TGC trigger stations are placed one before the middle MDT, and two behind, separated by about 2 m. There is only one station of CSC chambers, located close to the beam pipe, in front of the ECT. The end-cap chambers cover the range $1<|\eta|<2.7$.

The task of the MDTs, consisting of three layers of 3 cm diameter drift tubes, is to give a precise (~80 μm) radial position of muon tracks in the azimuthal direction in the end-caps and in the beam direction in the barrel. The basic RPC unit consists of a narrow gas gap formed by two parallel resistive bakelite plates, separated by insulating spacers. The goal of the RPC chambers is to provide the trigger function in the barrel region.

The trigger function in the end-caps is provide by TGC chambers, with wire and strip readout, the details of which will be presented in the next section. The strip readout, arranged in an orthogonal direction to the MDT tubes, is to provide the y coordinate for the precision measurement. The need for the second coordinate in the end-caps comes from the high occupancy, expected in all detectors in the forward region.

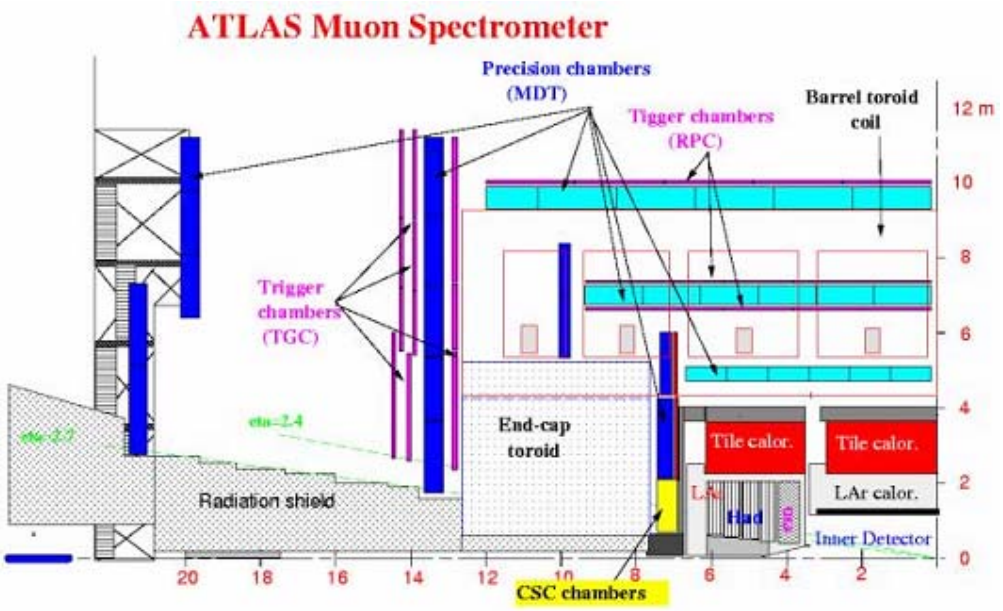

Fig. 5 : Muon chambers geometry relatively to the interaction point.

The muon momentum resolution of the spectrometer has been calculated using the three-dimensional field map of the toroid system. All known contributions to the measurement precision are taken into account, in particular alignment errors, multiple scattering simulated with a detailed description of the material distribution along a track, and energy loss fluctuations in the calorimeter. *Fig. 6* shows the expected resolution as a function of pseudorapidity.

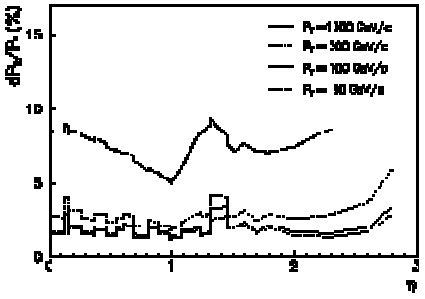

Fig. 6: Resolution of the muon transverse momentum, $\Delta P_T / P_T$, as a function of η, as expected from the measurements provided by the muon spectrometer.

For muons with momentum below 300 GeV, the resolution in the transverse momentum, $\Delta P_T / P_T$, is at a level of about 3% and fairly uniform in η.
For higher muon momentum, the resolution deteriorates to below 10% and depends on η.

4.2. Design of TGC chambers

The TGCs are similar in design to multiwire proportional chambers (ref), with the difference that the anode wire pitch is larger than the cathode-anode distance. They have been developed for the OPAL detector[6,7] and successfully operated in that experiment for several years. Thin gap chambers filled with CO_2 npentane mixture (55:45), operate in a saturated mode[8] at nominal high voltage 2.9 kV.

A schematic view is presented in *Fig. 7*. The anode plain is sandwiched between two cathode planes made of 1.6 mm G-10 plates on which the graphite cathode is deposited. On the backside of the cathode plates, facing the center plane of the chamber, etched copper strips provide the readout of the azimuthal coordinate.

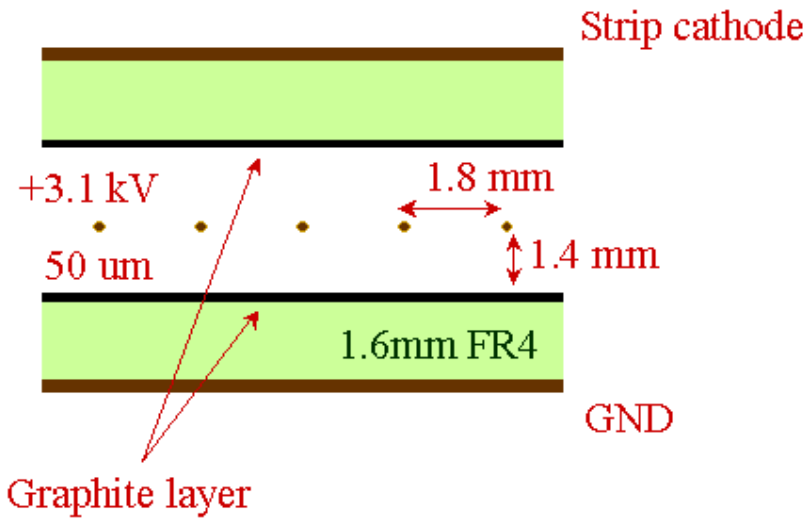

Fig. 7: Schematic view of a thin gap chamber

Signals from the anode wires together with readout strips arranged orthogonal to the wires provide the trigger information.
The chamber layout is shown in *Fig. 8* (the dimensions correspond to the so called T8 detector).

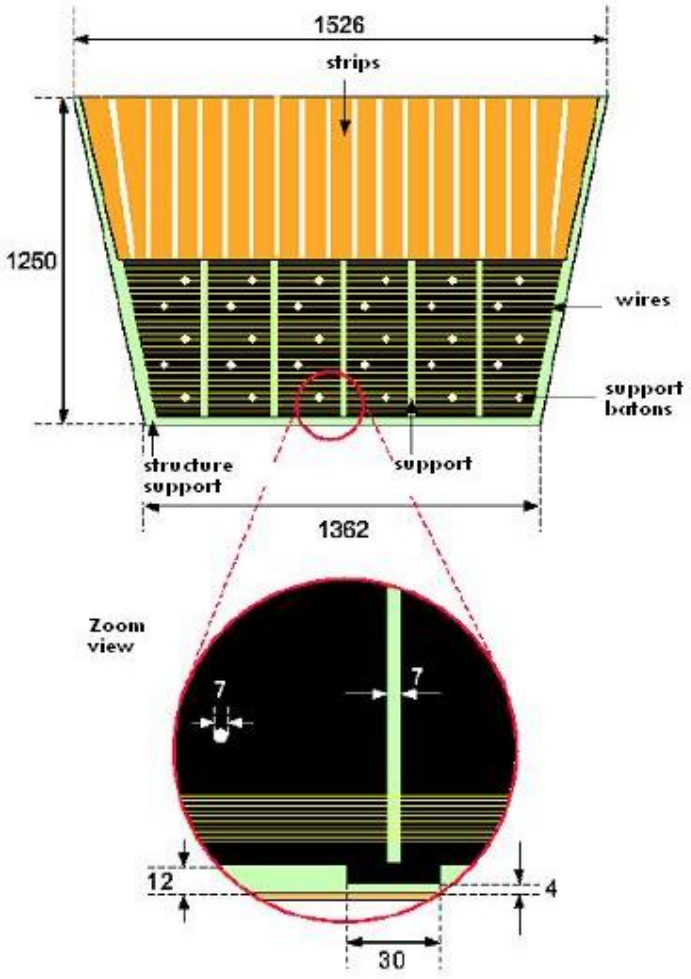

Fig. 8: View of a T8 TGC chamber from above. The upper yellow area depicts the geometry of the strips. The lower area, under the strips depicts the mesh of wires, perpendicular to the strips. The supports of the wires are also shown.

TGCs are characterized by:

- saturated-mode operation, leading to small Landau tails and a pulse shape from slow neutrons similar to that from minimum-ionizing particles;
- small sensitivity to magnetic field;

- fast signals with a typical rise time of 10 ns and r.m.s. time resolutions ≤ 4 ns;
- rate capability of up to 150 kHz/cm^2 without signal deterioration;
- full geometrical efficiency, except for a small area of dead space needed for wire supports (3-4%);
- strip and wire readout providing redundancy for position reconstruction.

One chamber has been irradiated with 10^{11} particles/cm^2 with no expected deterioration in response. This is equivalent to the exposure during three years of LHC operation at the highest rapidities covered by the muon spectrometer.

4.3. **Mechanical structure of TGC units**

The TGCs are constructed in units of doublets and triplets of TGC chambers. The inner station (M1) consists of one plane of doublets, the middle station (M2) of one plane of triplets, and the last one (M3) of two planes of doublets.

In a doublet, the TGC layers are separated by 20 mm thick paper honeycomb panel, which provides a rigid mechanical structure. On the outside, 5 mm thick paper honeycomb panels sustain the gas pressure. These are covered in turn by 0.5 mm G-10 plates. For the triplet TGC unit another wire plane is added.

In the ATLAS detector, the units are mounted on big wheels. The size of the various units depends on the radial position and the station number. There are 11 various units, namely from T1 to T11. The active area of the various chambers is changing from 1.31 m^2 to 2.27 m^2. The trigger TGC chamber covers an area of 3750 m^2 and the total number of the readout channels is 490000 (see next section).

The ATLAS TGCs are designed and built in Weizmann Institute in Israel in KEK in Japan as well as in Shandong University in China. The details of the production at the various sites are summarized in *Table 1*.

Country	*China*	*Japan*	*Israel*	*Total*
Place	Shandong Univ.	KEK	Weizmann Inst.	
# doublets	192	384	576	**1,152**
# triplets	-	96	336	**432**
Total	384	1,056	2,160	**3,600**

Table 1: The production distribution of the TGC units among the three construction sites.

There are three test sites to check the performance of the TGC units, two in Israel, at the Technion and at Tel-Aviv University, and one in Kobe University in Japan. The purpose of these tests is to provide a detailed map of detection efficiency and time resolution for each detector.

4.4. Principle of muon triggering with TGCs

The objective of the design of the muon trigger system was to use the momentum of muons produced in the interaction point of the ATLAS detector as signal. Muons with low angles with respect to the beam line cross the tracking device, shielding and calorimetry before they reach the TGCs. The muons emerging in the end-caps undergo Coulomb scattering and their tracks are bent by highly inhomogeneous magnetic fields. The goal of the trigger is to deduce from the TGC hits the transverse momentum, P_T, with which the muon was produced in the interaction point (IP).
The low-P_T trigger is based on M3 station only. A coincidence between two doublets of chambers is made within a road, the width of which is chosen to give 90% efficiency for $P_T \approx 6$ GeV. This is shown schematically in *Fig. 9*. Hits are required in three out of the four chambers, in each of the two orthogonal projections. The TGC low-P_T trigger is designed mainly for low luminosity runs.

At higher luminosity, a high p_T trigger will be activated. This trigger, with

a threshold of $P_T \approx 20$ GeV, will be based on the M2 and M3 stations, as shown in *Fig. 9*. If possible, also the low p_T trigger will be maintained.

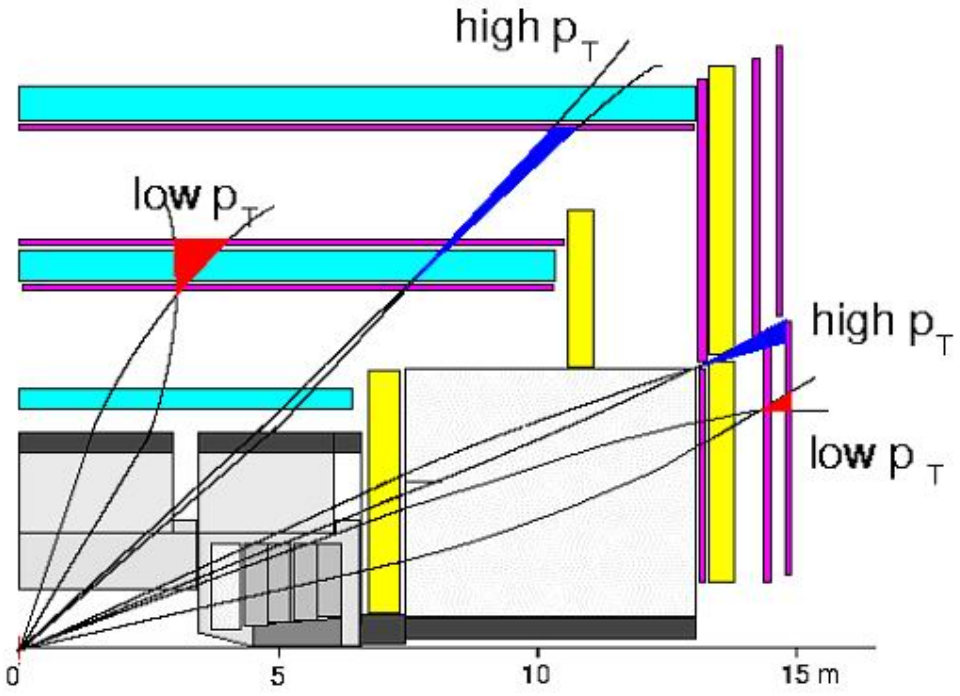

Fig. 9: A side view of one ATLAS quadrant. In black the muon trajectories. Both the barrel and the end cap muon trigger principle is depicted. The trajectories generated in the IP are shown for positive and negative muons.

4.5. The TGC readout

To form a trigger signal, several anode wires are grouped together and fed to a common readout channel. The number of wires per group varies between 4 and 20, with the former for high η and the latter for low η. The signals generated by TGCs are amplified, discriminated and shaped on the detector. The detector-mounted electronics first identifies the bunch crossing and then finds the hit coincidence independently in the radial and azimuthal roads.

Electronics situated outside the ATLAS cavern (the underground part of the detector) combines the measurements of the track coordinates in both directions, to make a trigger decision, which is then passed to the Muon Interface of the Central Trigger Processor, MUCTPI.

The wire and strip signals emerging from TGCs are fed into a two-stage amplifier in an Amplifier Shape Discriminator (ASD) circuit. Four such

circuits are built into a single ASD chip and four ASD chips are incorporated into an ASD Board; hence each ASD board handles 16 channels of signals. The ASD board is physically attached to the edge of a TGC chamber and enclosed inside the TGC electrical shielding. Signals from the ASD boards are sent to a Patch-Panel (PP), which houses receivers for the ASD outputs, to a Bunch Crossing Identification (BCID) circuits and the logic. The Patch panel also routes signals to and from the Detector Control System (DCS), and the muon end-cap trigger control and monitoring system and supplies power to the Slave Boards (SB). Outputs from the PP are sent to the corresponding SB, where the coincidence and readout circuits are placed. There are five different types of SB; the wire and strip boards for each of the triplet or doublet. They differ in their number of inputs, the kind of coincidence made for maximum road width. The hit information from the SB is sent to the Sector Logical Boards (SLB). The SLBs are located outside the main ATLAS cavern. The resulting trigger information is sent to the MUCPI. The total latency of the system, from the bunch crossing, in which the interaction occurs until the delivery of the level 1 track candidates to the MUCPI is 1.20 μs.

5. TGCs efficiency test

5.1. General description

In order to assure that all the TGC chambers (doublets or triplets) are working properly we follow three stages of quality control procedure.

- preliminary Checks,
- cosmic ray efficiency test,
- validation procedure.

Preliminary checks - Incoming TGC units are identified by their barcode number and are registered in the database. Than they go through a set of tests.

- **Mechanical integrity inspection.**
  A visual inspection of the incoming TGC units is performed to check that no mechanical damage was done.

- **Gas integrity of chambers.**
  Each TGC unit, that passed the mechanical inspection, is flushed with CO_2 at 40ml/min, for one day. Then, it is flushed with the operating gas (CO_2 -npentane mixture) for additional two days.

- **High Voltage check.**

After 48 hours of flowing gas mixture, the module is tested under HV. The HV is first ramped to the nominal 2.9 kV. If no trip is observed, the HV is further increased to the 3.1 kV, for the testing. At this voltage, the current of each counter has to be below $15\,\mu A$. No sparking should be encountered. The current and number of sparks (if any) is recorded in the database.

Cosmic ray efficiency test- Units that pass the preliminary tests, are moved to the Cosmic Ray efficiency bench test. The scope of this test is to measure the time response and the efficiency of the TGC counters. This is done with a cosmic rays telescope, schematically shown in *Fig. 10* and discussed in the next section. Accumulating events for a period of about one week, allows a full mapping of the efficiency of each detector in the stack, to a precision of 1%.

Validation procedure-For a chamber to pass the Cosmic Ray test, the efficiency over an active area of 95% should be above 95%. The time response is required to be less then 25 ns.

For each TGC unit (doublet or triplet) its barcode is read and the efficiency test results and other information for that unit is fetched from the database. If all the criteria are passed, an acceptance status is recorded in the database for future reference. If not, a rejection status is recorded.

5.2. Cosmic ray telescope

The telescope uses cosmic muons to measure the efficiency of the TGCs. The tested TGCs are sandwiched between two precision chambers (PRC). The PRC measure the impact point of the cosmic muon that crosses them. From this information, the track of the cosmic muons is reconstructed, and the crossing point through each plane within the stack of tested TGCs can be calculated. The number of times a signal was registered in a TGC, that was crossed by a muon, relative to the total number of crossing muons, defines the efficiency.

The information that a muon crossed the PRC and therefore the tested stack is provided by two scintillator planes, one above the upper PRC and one below the lower PRC. This is depicted in *Fig. 10*.

A coincidence between a hit in the upper scintillator plane and lower scintillator plane serves to trigger the data taking.

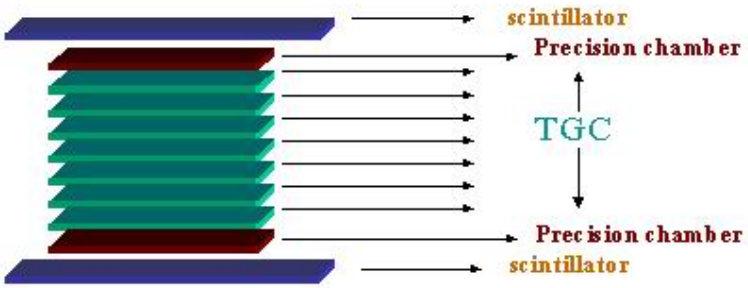

Fig. 10: The testbench schematic structure

5.3. Trigger signal

Each scintillator plane consists of four scintillator slabs, disconnected optically, 60 cm wide, 140 cm long, and 1.2 cm thick.
The scintillator material has a high index of refraction (n=1.58), and it is polished accurately to have total reflection, not allowing light produced inside to escape. The emittance spectrum of the scintillator material is shown in *Fig. 11*. A seen in the figure, the entire spectrum is in the visible range.

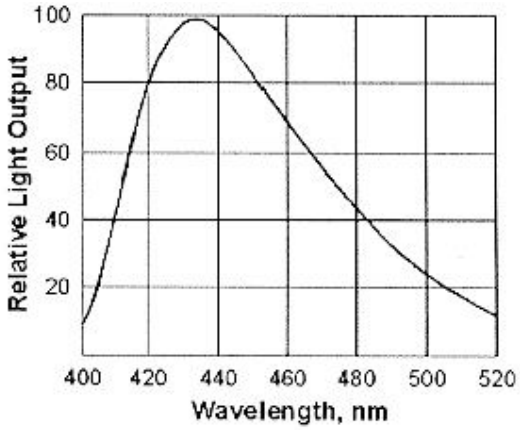

Fig. 11: The emitance spectrum of the scintillator material.

The two ends of the scintillator slab are connected to triangular light-guides that guide the collected light to respective PMTs.
We use Hamamatsu R329-02 PMTs, which are active in the range of 300-650 ns and rise time of 2.6 ns. The corresponding absorption spectrums for the PMTs are shown in *Fig. 12*.

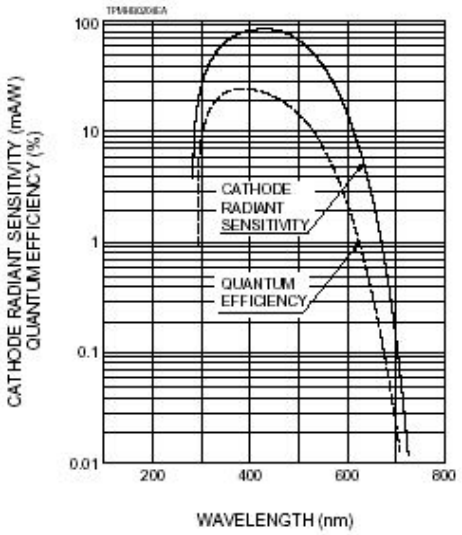

Fig. 12 : The working spectrum of the PMT.

The geometry of a single scintillator detector consisting of a scintillator slab, two lightguides and two PMTs, is depicted in *Fig. 13*.

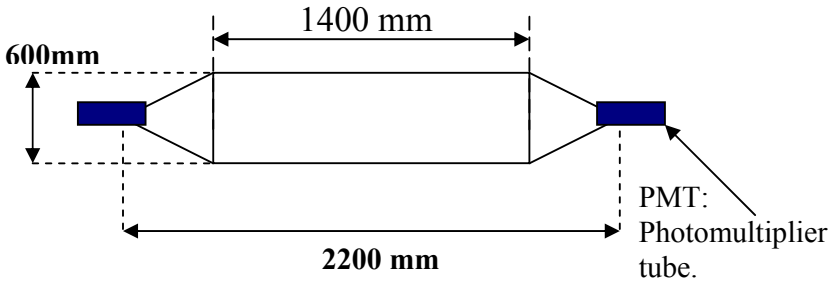

Fig. 13:The structure of one scintillator detector.

The scintillator lightguides and photomultiplier tubes are carefully wrapped with black sealed plastic and tape to avoid that external light source triggers the system. As an illustration, two scintillator detectors, one after wrapping, one before, are shown in *Fig. 14*.

Fig. 14 Picture of scintillator slabs with their lightguides. One of them is already wrapped with black plastic sheet and two phototubes are seen as well.

5.4. Precision chambers

The precision chamber has a square shape, and consists of two layers of strips and one layer of high voltage wires between them (see *Fig. 15*). The strips from the layers are perpendicular to each other. There are 361 strips along the X-axis of the square, and 458 strips along its Y-axis. Each strip has a width of 3.6-mm. The signals from the two layers are latched and read sequentially providing the X and Y coordinate of a hit position.

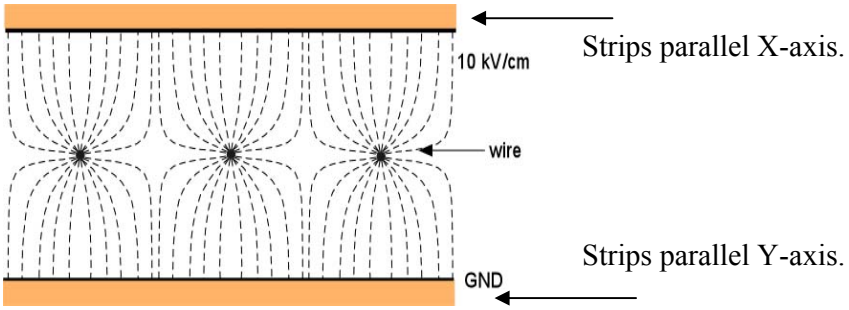

Fig. 15: The structure of the precision chamber.

5.5. The gas system

The precision chambers and the TGC detectors need a constant gas flow. The gas system produces a mixture of 45% npentane and 55% of CO_2, which prevents discharges in the chambers. This mixture is achieved by bubbling CO_2 gas through liquid npentane at temperature of 17^0 C. A single gas supply line carries about 20 l/h of the gas mixture from the gas mixing system to the detectors.

5.6. The readout scheme

The following electronic units are installed on the chambers:

- ASD board – it is an Amplifier Shape Discriminator (ASD) board, attached to the edge of a TGC chamber and enclosed inside the TGC electrical shielding.
- Gassiplex chip – developed at CERN, it reads and amplifies the signal from each strip channel, to which it is connected by a protection card. This card protect the Gassiplex from high currents

A VME bus is used as a common interface between a CPU and the lab measuring equipment. The following cards are connected through the VME bus:

- A CPU module. This is a 1Ghz Pentium III running Linux operating system, with 256 MB SDRAM. It includes all standard PC I/O (keyboard, mouse, SVGA, IDE, FDC, COM1/2, LPT1), a Flat Panel, 10/100BaseTX, Fast/Wide SCSI-2, VME64 support; optional transition module CD-ROM/floppy and IDE hard drive.
- TDC – CAEN V767. This is a multi-hit time to digital converter (TDC), a one-unit wide VME module, that houses, four chips, each with 32 time to digital conversion channels (128 channels in total).
- C-RAM – CAEN mod. V550. This is an analog to digital converter (ADC). C-RAM is a one-unit wide VME module housing two independent analog to digital conversion blocks.
- SEQUENCER – CAEN mod. V551B. This is a one-unit wide VME module that handles the Data Acquisition from the PRC. The SEQUENCER has been developed to control the signals from/to the C-RAM boards.
- HV – CAEN, it is a High Speed VME Controller Interface mod. V288. This unit is used to control the HV distribution to the scintillator and the chambers.

The following units are connected to NIM crates:

- NIM - TTL – CAEN, NIM Adapter mod. N89. This module is housing two sections of 4 NIM to TTL converters and two sections of 4 TTL to NIM converters.
- NIM - ECL adapter – it is designed by the Technion to convert the NIM standard to ECL standard.
- ASD readout board – made in Technion, reads the signals from the on-chamber ASD boards.

- ASD-TDC unit – made in Technion. It is an adapter of the ASD readout signals (NIM) to the standard of the TDC card (ECL).
- DISCRIMINATOR – LeCroy. It is a constant fraction discriminator, which generates precise digital logic pulse, from an analog one, if the latter exceeds a given threshold.
- OR/AND logical units – LeCroy. Each unit may generate an AND or an OR signal between two signals.

The signals from the scintillators are used to trigger the system and set a time reference to the measurements. The connection of the signal coming from the PMTs is shown in *Fig. 16*. The eight PMT signals of each scintillator plane after discrimination, are connected to an OR unit. The output of the two OR units are then passed to an AND logical unit, whose output serves as a trigger signal for the readout system.

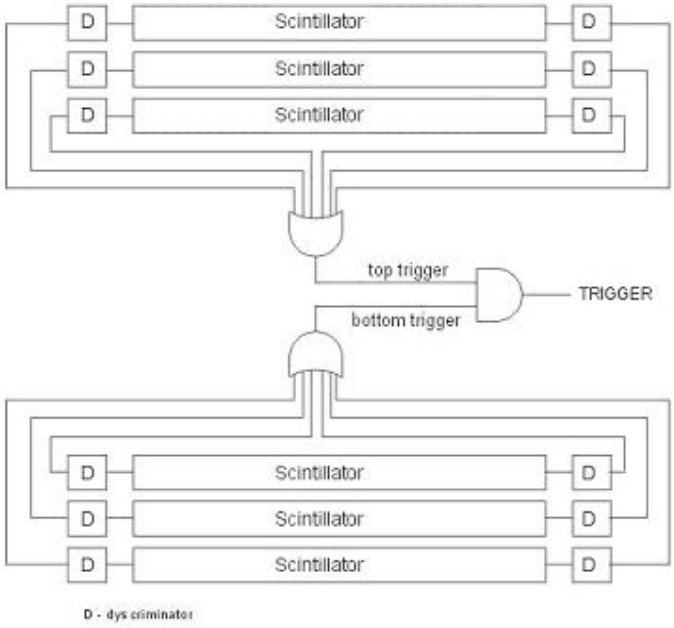

Fig. 16: Schematic diagram of connections between the scintillators.

The signals from the OR units, after being delayed by 100 ns and passed through the NIM-ECL converter, are connected to the TDC unit, via the ASD-TDC card.

The signals from the TGCs go through the ASD, the ASD readout board and the ASD-TDC converter to the TDC. This route is necessary to measure the time response of each TGC chamber.

The electronic connections of the PRC are as follows:

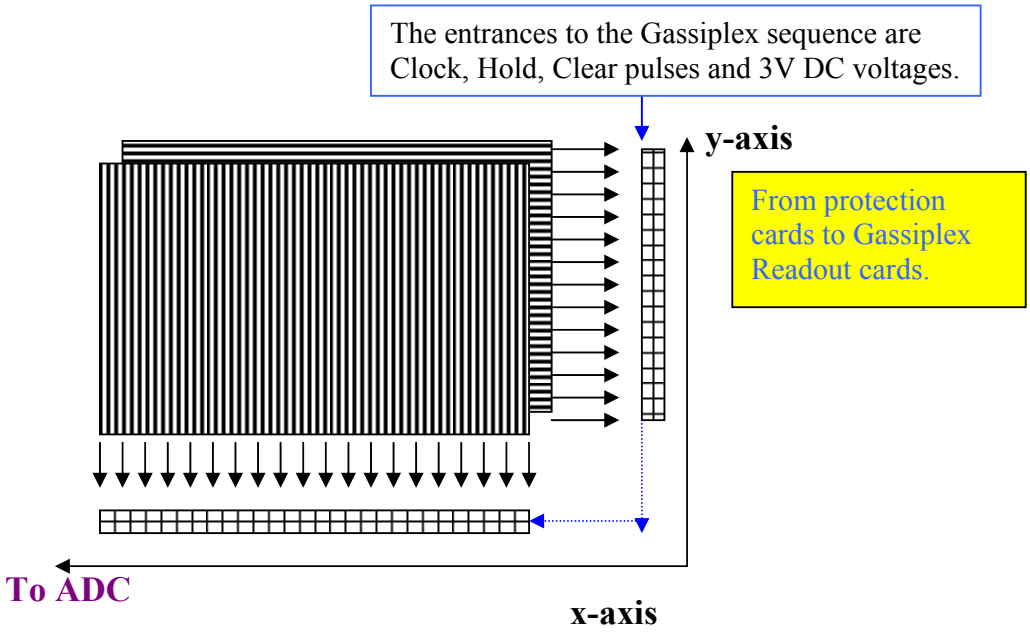

Fig. 17:The electronic connection of the precision chamber.

The Gassiplex unit provides the PRC signals to the ADC unit as shown schematically in *Fig. 17*.
The Gassiplex uses a serial reading mode. Its entries are the CLOCK HOLD and CLEAR signals that are generated by the SEQUENCER. The CLOCK determines the time length for reading one channel. The HOLD signal freezes the information that is currently in the Gassiplex chip; the CLOCK pushes the signal to the output (C-RAM) and then a CLEAR signal resets all Gassiplex chips.

The electronic connections between all the different units in the readout systems are schematically depicted in *Fig. 18*.

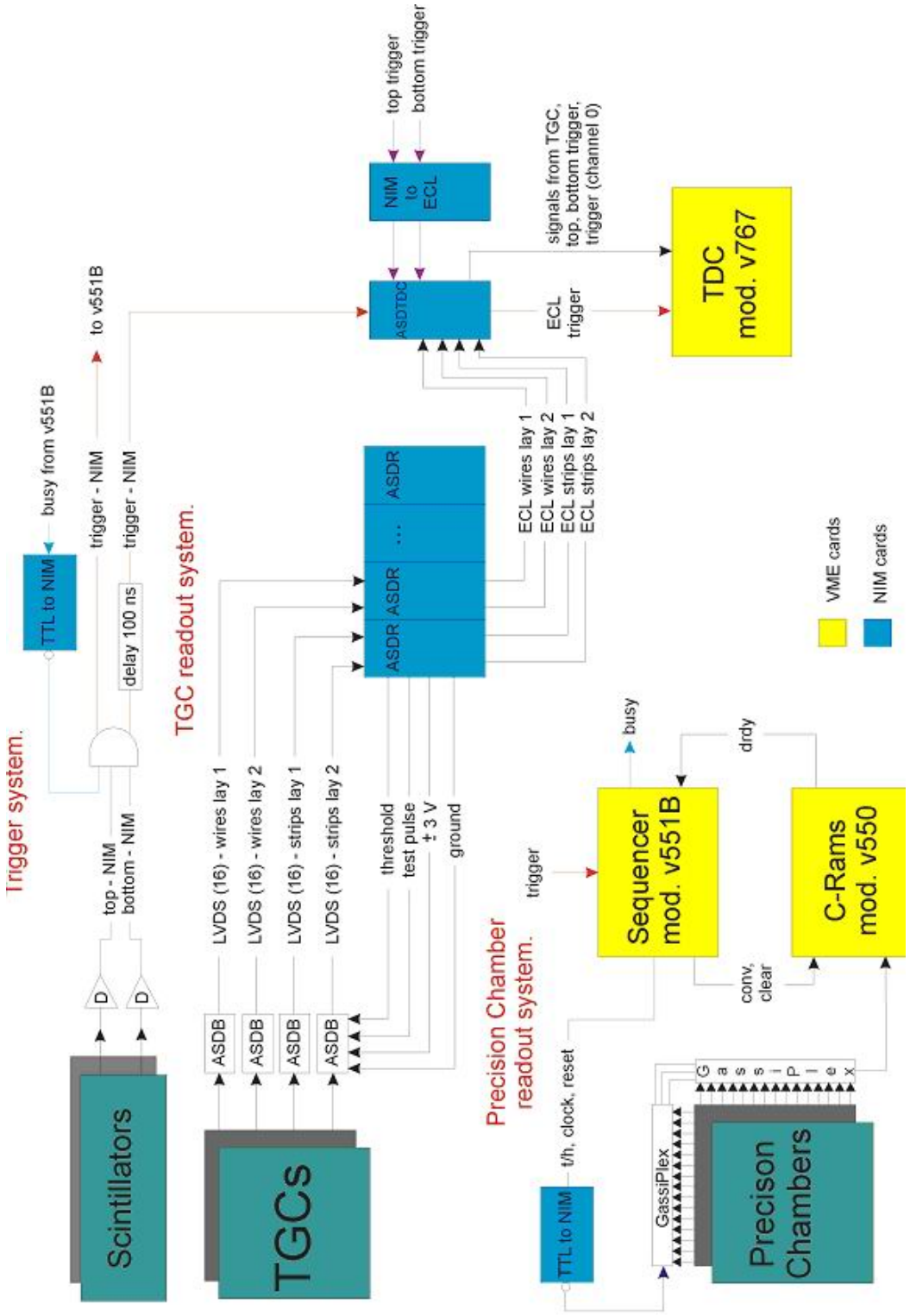

Fig. 18: The layout of the readout system.

5.7. The online readout software

The Online program reads the data from the TDC, the ADC (C-RAM), and the HV controller, and stores the data in a binary output file for further off-line analysis.
The structure of the Data Acquisition (DAQ) flow is shown in *Fig. 19*.

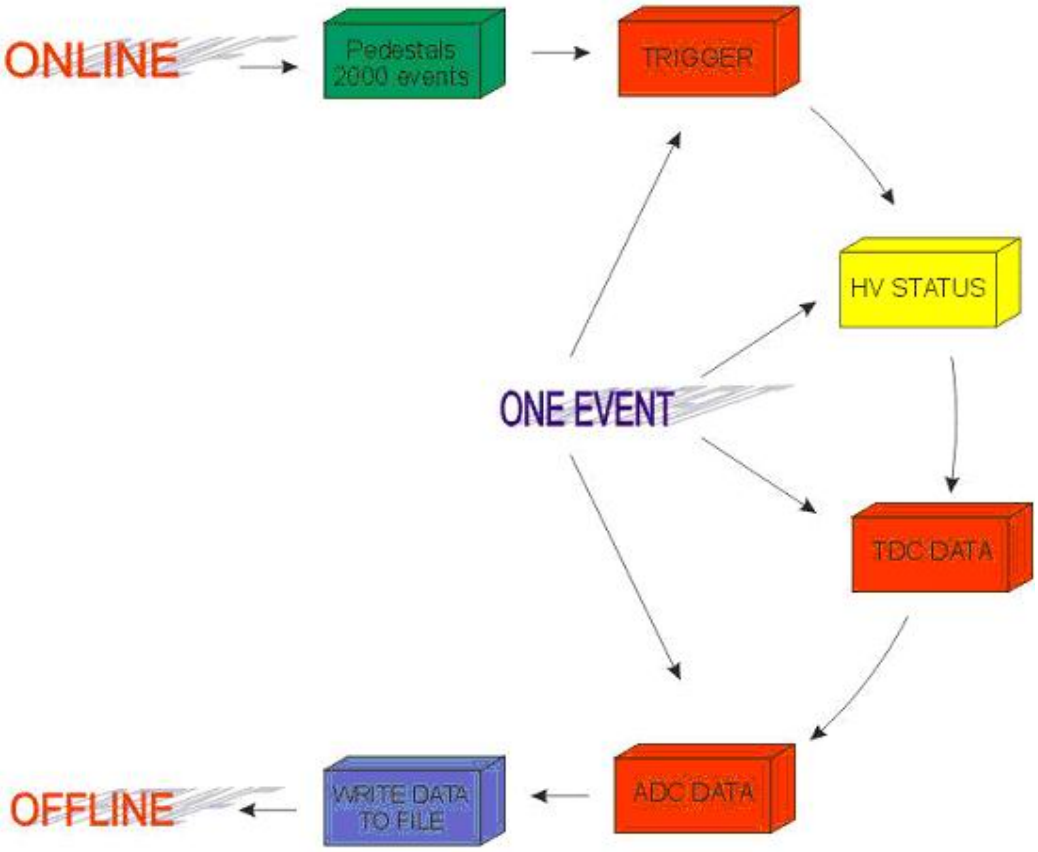

Fig. 19: The Data Acquisition flow.

The online DAQ program has several stages of operation:

- Pedestals and Thresholds, for PRC readout. At the beginning of the run the program sets a memory of pedestals and thresholds for the PRC channels. The program reads 2000 events with a software generated random trigger, thus providing mostly noise level. For each cannel the average noise level, P_{ch} and its

uncertainty, σ_{ch} are calculated. The threshold for each channel is then set to $p_{ch} + N\sigma_{ch}$ where is N chosen to be 3.3, as a result of optimising the efficiency and the purity for reconstruction real muon tracks.

- Data acquisition. If a trigger is detected the program reads the data from the VME cards, from the HV unit, the TDC unit and the ADC units. The program runs simple validation checks on the data before they are written out.
- Output. The Online code writes its output into a binary structured file for the offline analysis stage. In parallel program writes out additional ASCII files, which contain data for continuous on-line monitoring of data quality and the equipment performance. (See Appendix I)
- The data are stored into files of one million events, for which typically seven hours of running are needed.

6. Analysis

An offline analysis program written in the object-oriented language, C++, reads the results of the online code and processes them. The purpose of this program is to calculate the TGC chambers time response and efficiency.
As far as the TGC timing is concern, it is required that for each channel (wire or strip) in 99 % of the events, the signal arrives within 25 ns relative to the trigger.
The binary data file, that Online program writes, contains for each event the hits above thresholds in the ADCs and the timing information of the TGCs hits (eight TDC channels for the doublet and twelve channels for the triplets), the trigger and the time of the hits in the top scintillators and the bottom scintillators.
Information about the HV status is passed once every 5000 events. The Offline program reads the data from the binary files and store it in separate structures.

At the beginning of its run the analysis program reads the header of the binary file, which contains information about the geometric setup and the electronic connections in that run. This includes:

1. The Scintillator detectors. Their vertical positions and the corresponding TDC channels connections.

2. The PRCs. Their vertical positions and the ADC channels connections.
3. The general setup of the testbench: numbers of the channels of ADC, TDC, and HV power supply values.

Another text file that the analysis program is reading contains information about the type of tested chambers (doublets or triplets), the geometric setup (z coordinates) of the TGCs and there electronic connections to the TDC.

6.1. Study of the test-bench timing

6.1.1. Scintillator time calculation

PMT

Fig. 20: Detecting the generated photons in the scintillator.

The photons produced when a muon crosses the scintillator material can be detected in each of the two PMTs on the two sides of the scintillators. To study the time response of the scintillator detectors we calculate the difference between the arrival times of the signal in the left and right PMTs.

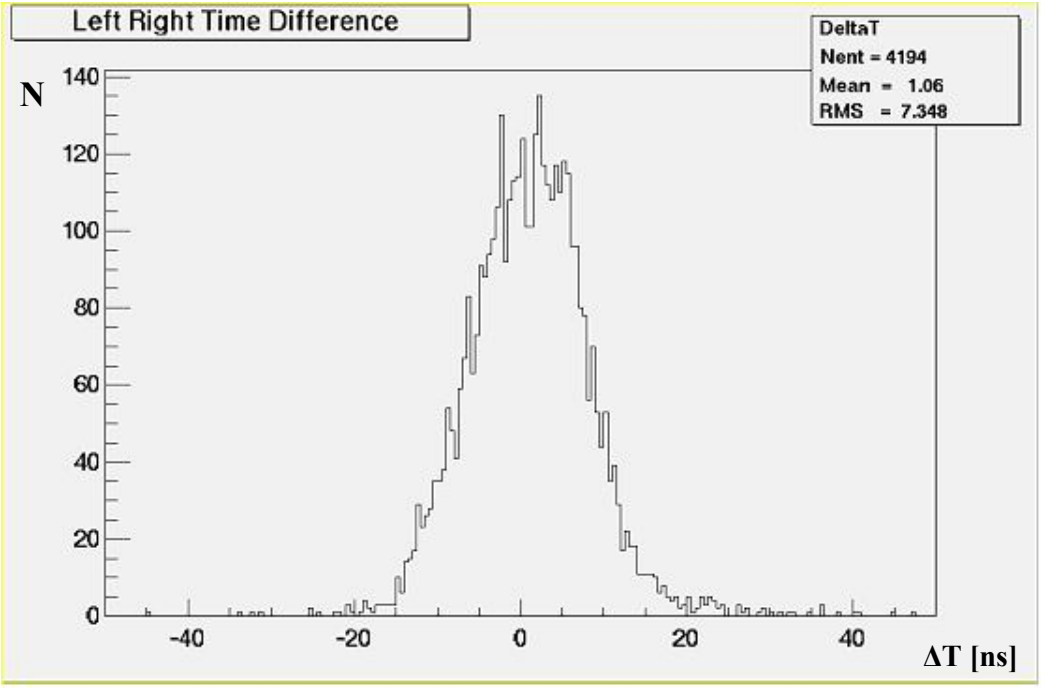

Fig. 21 : The time difference between left and right sides of the scintillator detector.

The difference, ΔT, is shown in *Fig. 21*. The expected maximum difference, due to geometrical considerations, is 3 ns. The observed difference extends to 20 ns and more. The manufacturer's specification of the time response of the PMTs is 4 ns. This still does not account for the measured difference, which is too large to allow meaningful studies of the TGC timing.

Beside the factors already mentioned the distribution width depends on other factors:

- The time propagation in the scintillators;
- The time response of logical gates, which are used to generate the trigger.
- The time response of the TDC, itself.

We conclude that different operating voltages of the PMTs do not change the width of ΔT. Different setup for the logical gates did not change the width of the ΔT distribution either.

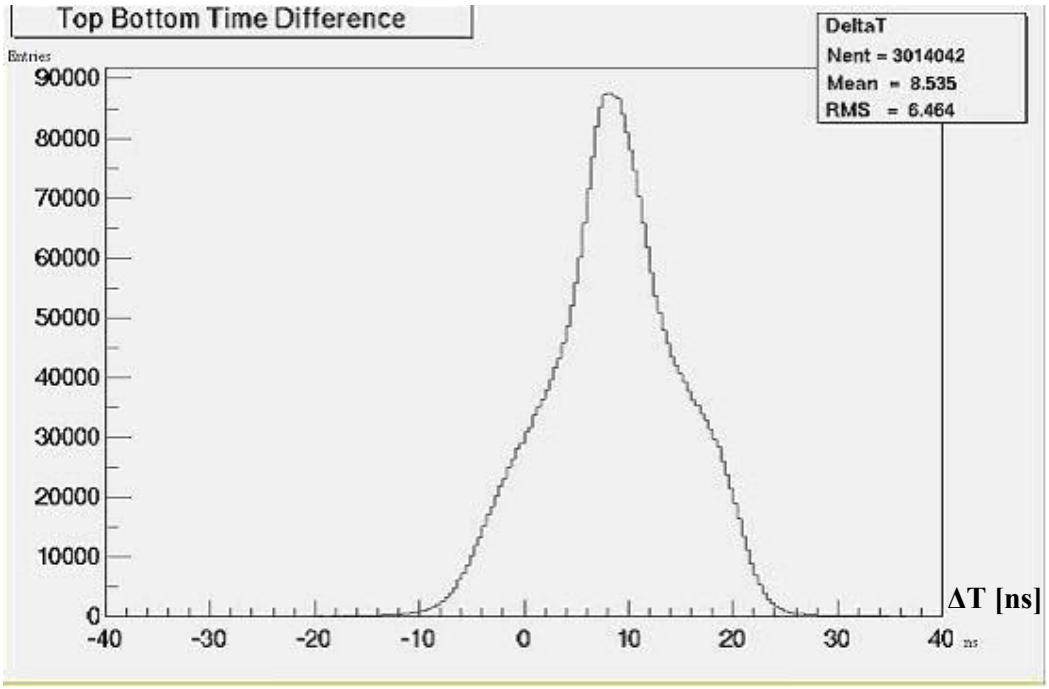

Fig. 22: The Top scintillator time minus Bottom one.

Fig. 22 shows the distribution of the time difference between the arrival time of the signal in the top and the bottom scintillator layers. The time difference **ΔT** is centered around 8.5 ns, which can be explained by the distance between the two scintillator layers. For vertical muons, **ΔT** is expected to be 7 ns. However the width of the distribution is much larger than expected. Moreover we observe negative values of **ΔT**, which, assuming that there are no muons coming from below, would mean that the time propagation in the scintillator can be as long as 17 ns. This is far from the estimated 3 ns.

As it turned out the bad resolution of our scintillators timing comes from an inhomogeneous behavior of the NIM (digital signal with of 800mV amplitude) to ECL (digital differential signal with ±800mV amplitudes as accepted by the TDC unit) converter we are currently using. This is demonstrated in *Fig. 23* where we plot the measured time difference between two signals generated 40 ns apart by a pulse generator.

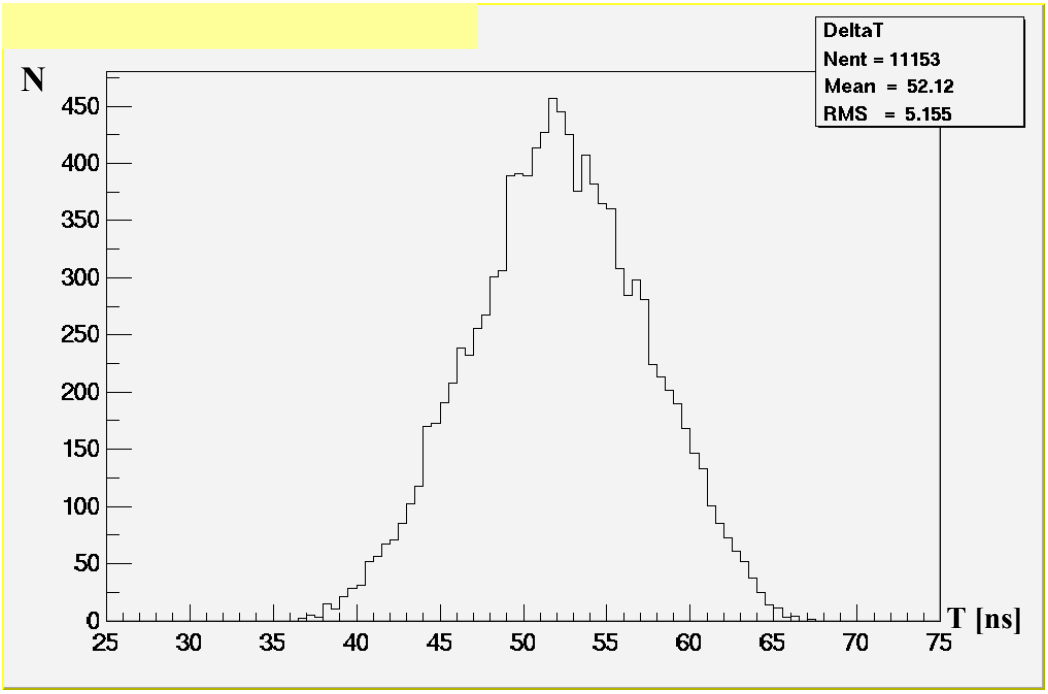

Fig. 23: The time difference between pulses originally generated with 40 ns gap between them.

The time difference is measured to be on average 52 ns instead of the input 40 ns. The NIM-ECL converter spreads the timing by 12 ns, with an RMS of 5 ns. This could very well account for the effect that we observed in *Fig. 22*.
By replacing NIM-ECL unit and adding extra unit to measure the timing of each PMT, we expect to improve the timing performance.
We conclude by stating that at this stage we are unable to study the timing of the TGCs and will therefore concentrate on their geometrical efficiency.

6.2. Muon reconstruction

6.2.1. Selection of one-muon candidates

In order to ensure that only one track crossed the TGC stack, only those events are selected in which there is only one cluster of adjacent strips in each direction, in each PRC. The distribution of the number of strips in a cluster is shown in *Fig. 24*.

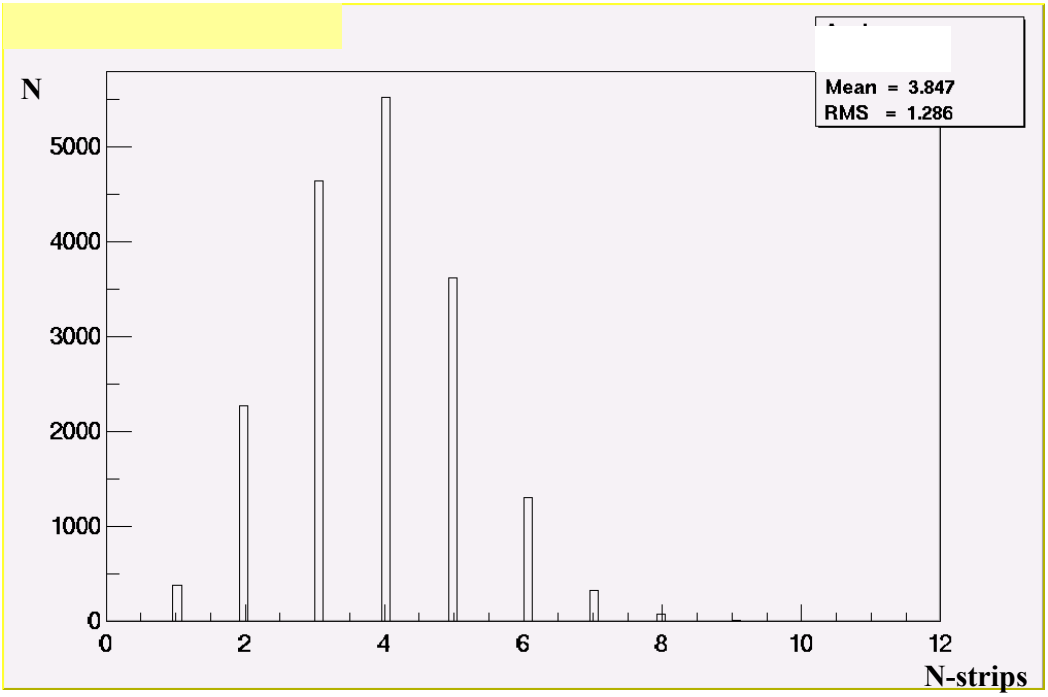

Fig. 24: The distribution of the number of strips per event.

A single event, on average, is distributes over 3.8 strips, while all the events have less than 11 strips.

In total four coordinate points need to be reconstructed. The following procedure is applied. For a given direction, assumed to be x for simplicity, the total pulse height (pedestal subtracted) is calculated, P_{tot}, as well as, the center of gravity of all strips, $\overline{x}_{tot}$,

Eq. 1

$$P_{tot} = \sum_i P_i;$$

$$\overline{x}_{tot} = \frac{\sum_i x_i P_i}{P_{tot}};$$

In the next step, the pulse height contained within a restricted range of ±5 strips of the strip containing $\overline{x}_{tot}$ is calculated, P_{sub}. If $P_{sub} < 0.9 P_{tot}$ the event is rejected. The distribution of P_{sub} / P_{tot} is depicted in *Fig 25.*

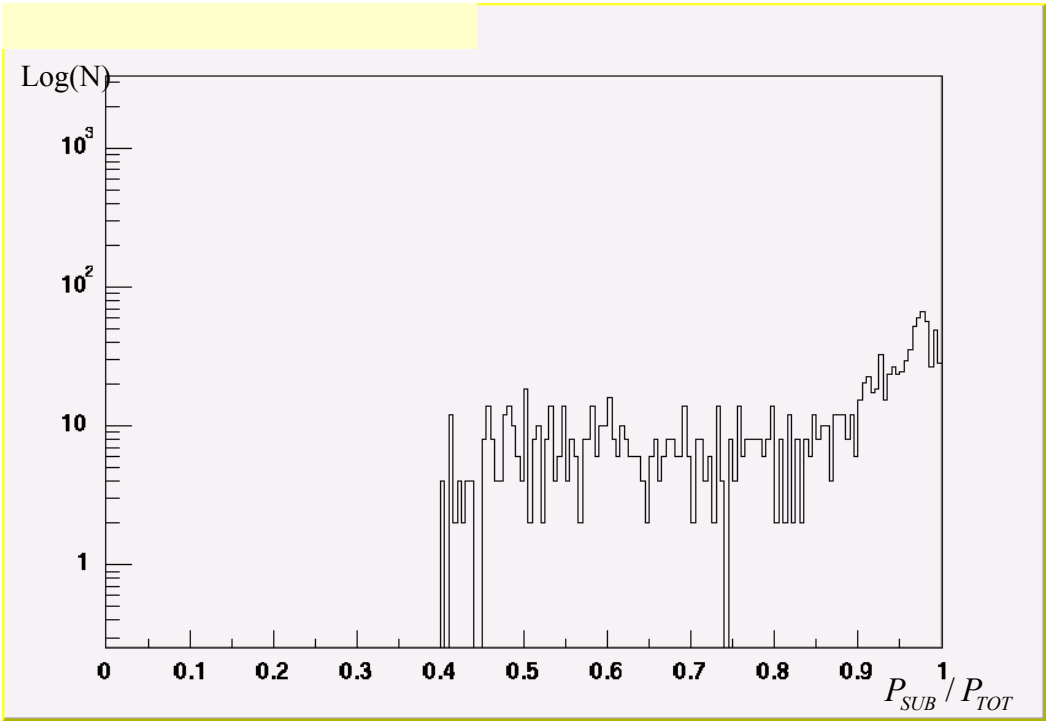

Fig 25: A logarithmic distribution of the ratio of P_{SUB} *over* P_{TOT}.

Noise in the PRC readout scheme can result in a cluster that distributes over more than 11 strips or produces two separated clusters. Those events are rejected by the selection process.
After requiring that there is enough information to reconstruct the (x, y) position of the muon crossing in the top and the bottom PRC, 64 % of events are rejected. Some statistics on the selection procedure is collected in *Table 2*.

Tel-Aviv University Precision chambers.	
Total number of events is 250000	N. events (in %)
The top precision chamber.	
No data on X axes	23 %
No data on Y axes	20 %
Double hit on X axes	5 %
Double hit on Y axes	4 %
Good data on X axes	68 %
Good data on Y axes	69 %
Only X event	6 %
Only Y event	7 %
The bottom precision chamber.	
No data on X axes	25 %
No data on Y axes	19 %
Double hit on X axes	2 %
Double hit on Y axes	3 %
Good data on X axes	66 %
Good data on Y axes	68 %
Only X event	7 %
Only Y event	9 %
Only event in the top precision chamber.	62 %
Only event in the bottom precision chamber.	59 %
Good data in the top and the bottom precision chambers.	36 %

Table 2: Statistics of rejected or accepted events at various stages of the selection procedure.

6.2.2. Position reconstruction

The pulse height distribution for a hit in PRC is expected to have a Gaussian like distribution. The profile of the voltage measured in the strips is depicted in the *Fig 26.*

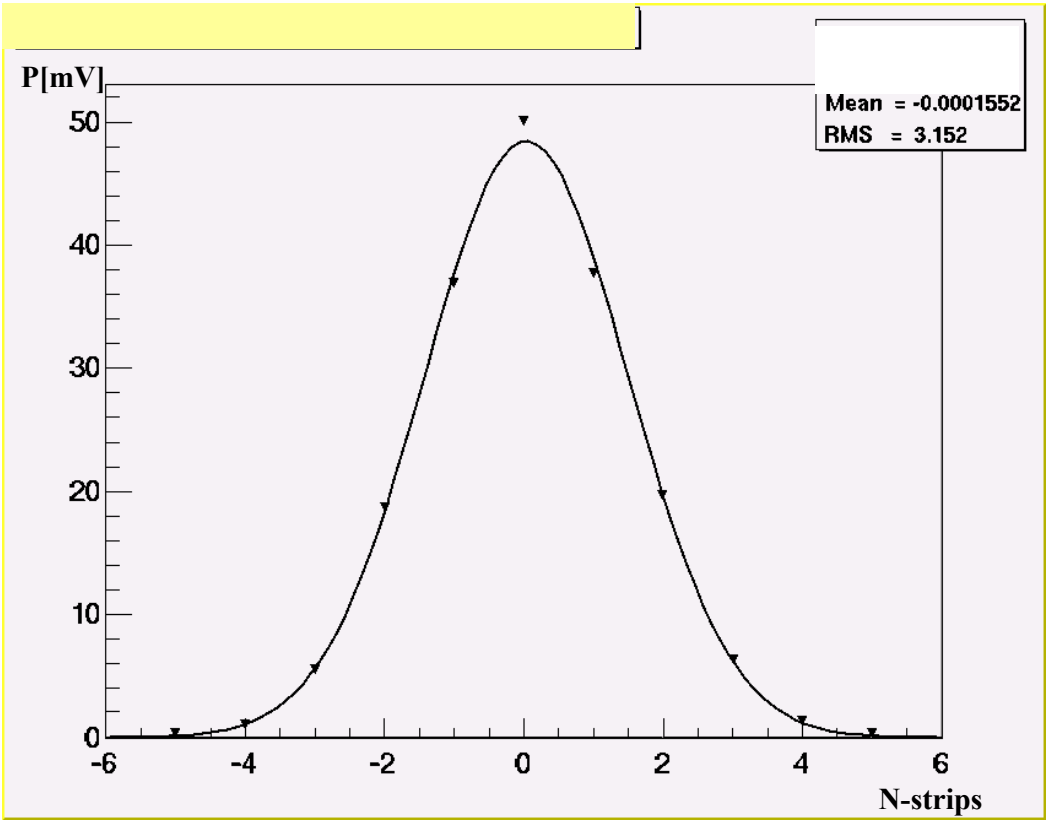

Fig 26: The average distribution of the voltage in the PRC strips, around the strip in the cluster with the maximal voltage, denoted as zero in the figure.

The procedure of fitting a Gaussian for each event is very involved. Instead we explored the accuracy achieved by using a simple weighted average. For a sample of events both methods were used and the results compared.

For the Gaussian fit, the Gaussian distribution was integrated over the strip size. The values of the fitted mean position, $\bar{x}_G$, and of the corresponding error were recorded. For the weighted average,

Eq. 2
$$\bar{x}_W = \sum_i x_i P_i \Big/ P_{sub} ,$$

the accuracy is given by,

Eq. 3
$$\Delta\bar{x}_W = \sqrt{\sum_i (x_i - \bar{x}_W)^2 \cdot (\Delta P_i / P_{sub})^2}$$

where ΔP_i depends on the fluctuation of the signal in a single strip ($\Delta P_i = \sqrt{P_i}$). In *Fig 27*, the difference $\overline{x}_W - \overline{x}_G$ is plotted.

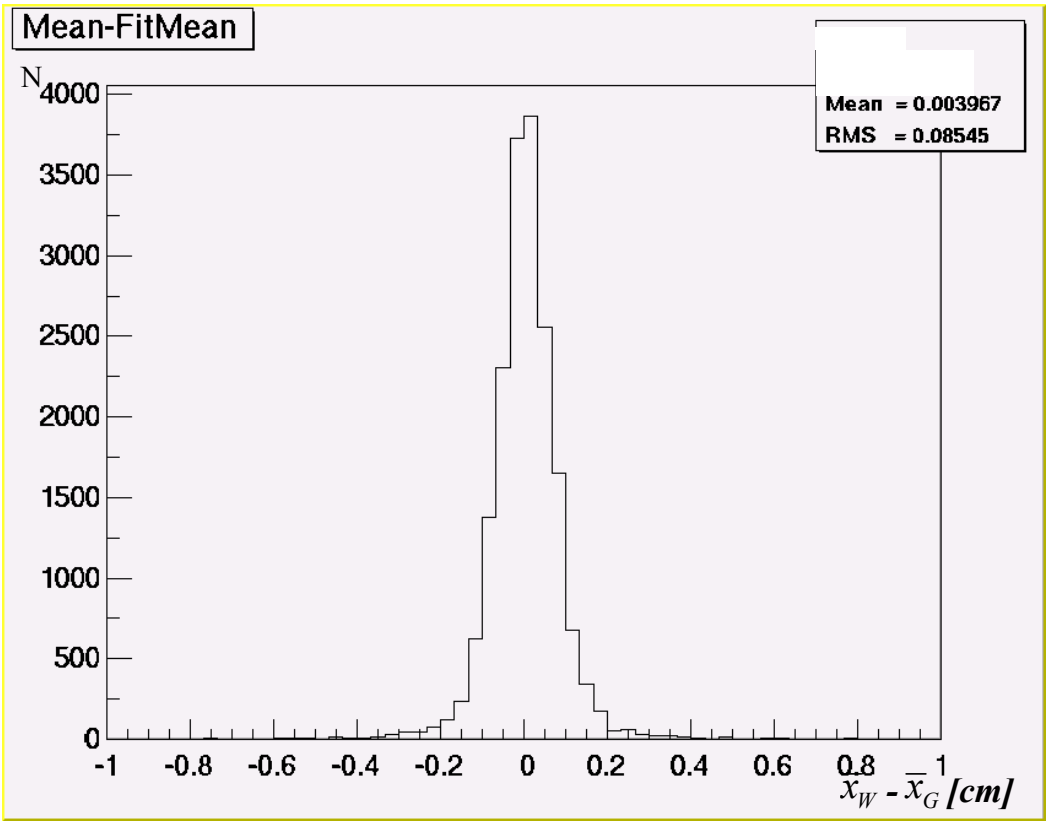

Fig 27: The distribution of the difference $\overline{x}_W - \overline{x}_G$.

As expected the distribution is centered around zero. The RMS of the distribution is well below the bin size (1 cm^2) and therefore the estimate of the position through $\overline{x}_W$ turn out to be, as good as through $\overline{x}_G$.

We conclude that the simple weighted average provide, a good approximation for the position measurement.

6.2.3. Trajectory calculation

To derive the intersection position with the TGCs, the fact that the muon is a weakly interacting particle is used, and it is assume that the charged muon crossed the PRC and the TGC planes in a straight line. At this stage multiple scattering effects are neglected.
The intersection position with the TGC is derived in the following way:

1. The coordinates of the two hits in the top and bottom PRC,(x_2,y_2,z_2) and (x_1,y_1,z_1) respectively are calculated.
2. The parameters of the straight line connecting the two space points are calculated, assuming the errors are identical.

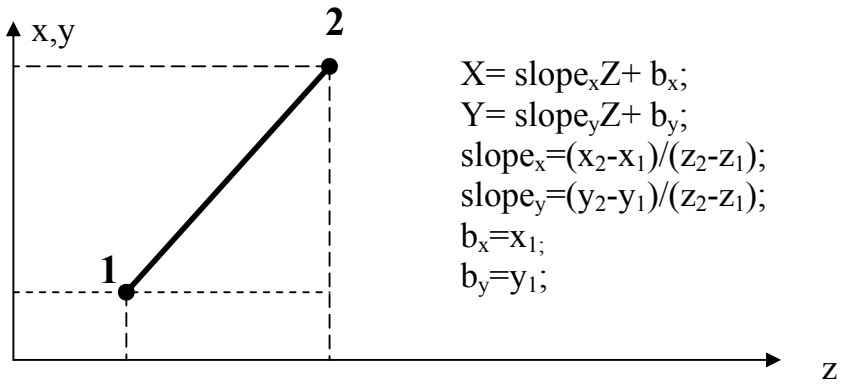

Fig. 28: The equation for the line connecting the two coordinates.

The intersection point with each TGC plane is calculated using the following relations:

$$x_{TGC} = slope_x \cdot (z_{TGC} - z_1) + b_x;$$

Eq. 4

$$y_{TGC} = slope_y \cdot (z_{TGC} - z_1) + b_y;$$

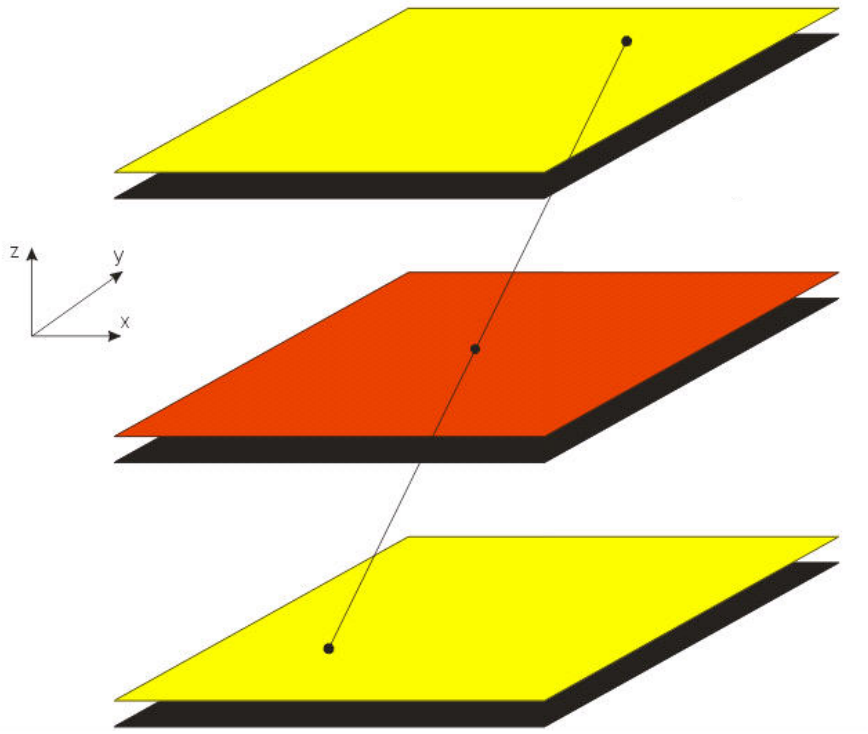

Fig. 29: Trajectory calculation. In yellow the top and bottom precision chambers, in red a TGC plane.

6.2.4. Systematic error uncertainties

The study of the errors in $\mathbf{X_{TGC}}$ **and** $\mathbf{Y_{TGC}}$ is aimed at learning the systematic limitation of the position measurement.

The distribution of the error Δx as defined in *Eq. 3* (where here x stands for $\mathbf{X_{TGC}}$ **or** $\mathbf{Y_{TGC}}$) is plotted in *Fig. 30*.

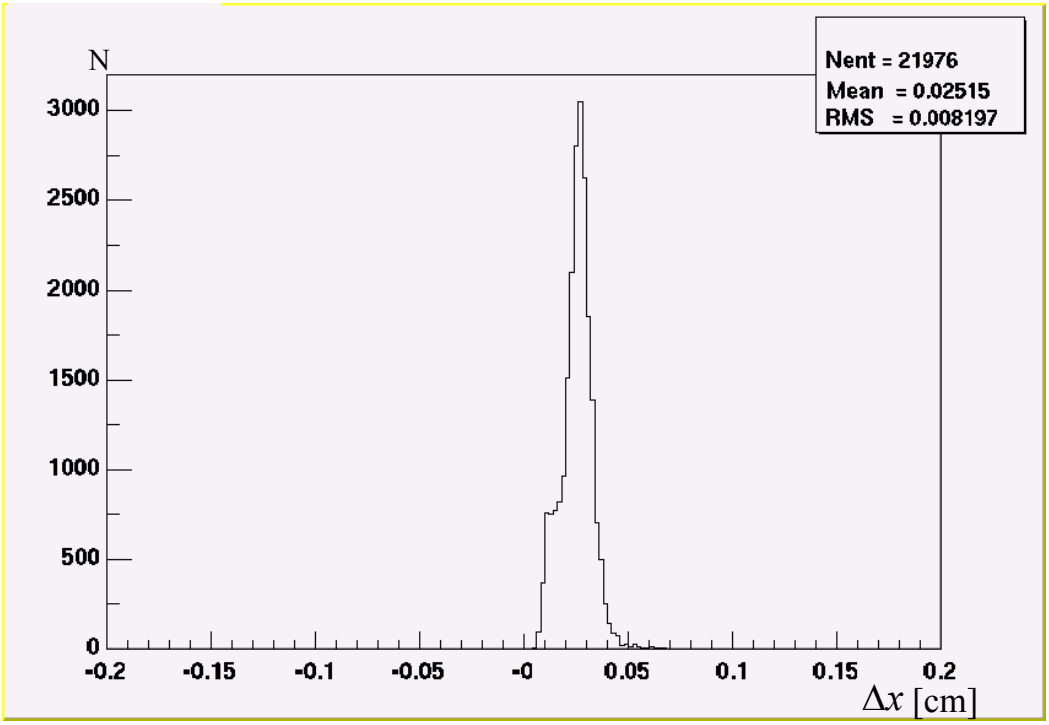

Fig. 30: The distribution of the error in position difference Δx .

The mean value of the distribution is 0.25 mm with RMS of 0.08 mm. This value is well below the resolution of our position measurements with a bin size of one cm^2.

Other effect that can impact the error on the position measurements is multiple scattering. To study its impact we run a toy Monte Carlo (MC) of minimum ionizing particle crossing the testbench (see Appendix II). The result of this study is the distribution of the extrapolation uncertainties as presented in
Fig. ***31***.

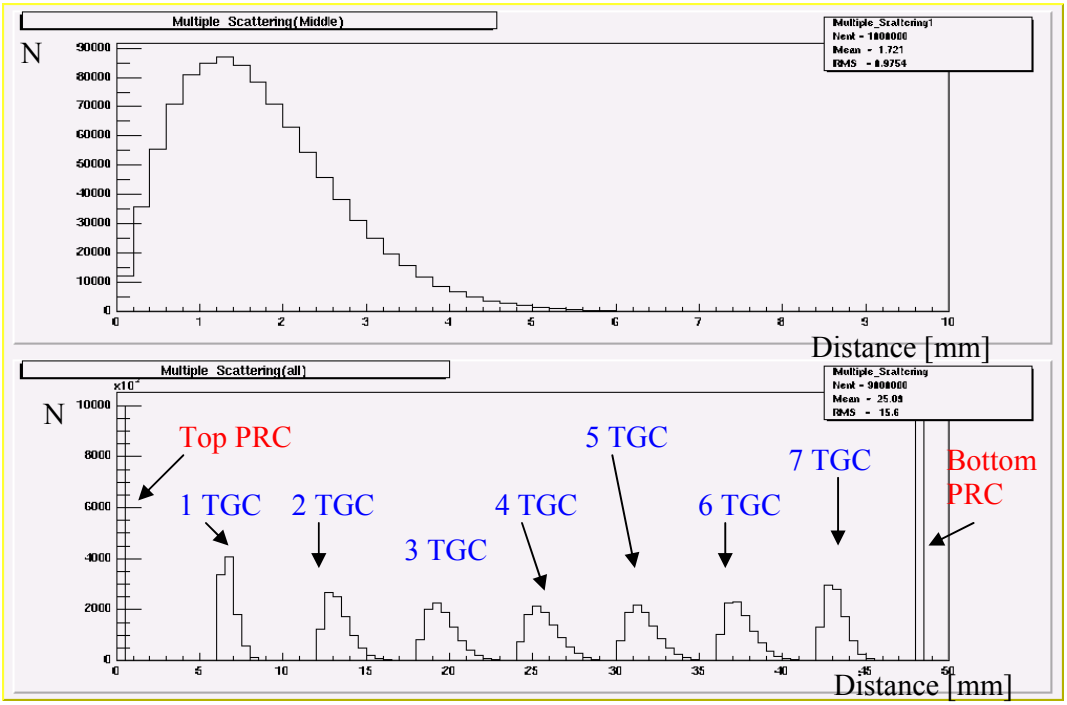

Fig. 31: Top histogram is the distribution of the distance between the measured hits in the TGC, placed in the testbench center, and the extrapolated ones. The bottom plot contains nine histograms. Each of which represents the error distribution for a certain layer in the testbench.

Fig. 31 (bottom figure) shows the extrapolation errors distribution for each of the seven possible TGC layers in the testbench. Since the position of the crossing point is actually measured in the PRCs at the two ends of the testbench (TGC 1, TGC 7)the extrapolation yield better precision next to the ends where it is clearly seen that the distribution gets wider the closer we get to the center of the testbench (TGC 4).
The two lines in the corners stand for the top and bottom RPCs with no extrapolation errors. On *Fig. 31* top we can see a zoom of the distribution of the middle TGC (TGC 4). As expected this unit has the largest extrapolation uncertainty of 1.72 mm with RMS of 0.97 mm.
This is well demonstrated in *Fig 32*. There we plot the width of the uncertainty distribution as a function of the TGC position in the testbench.

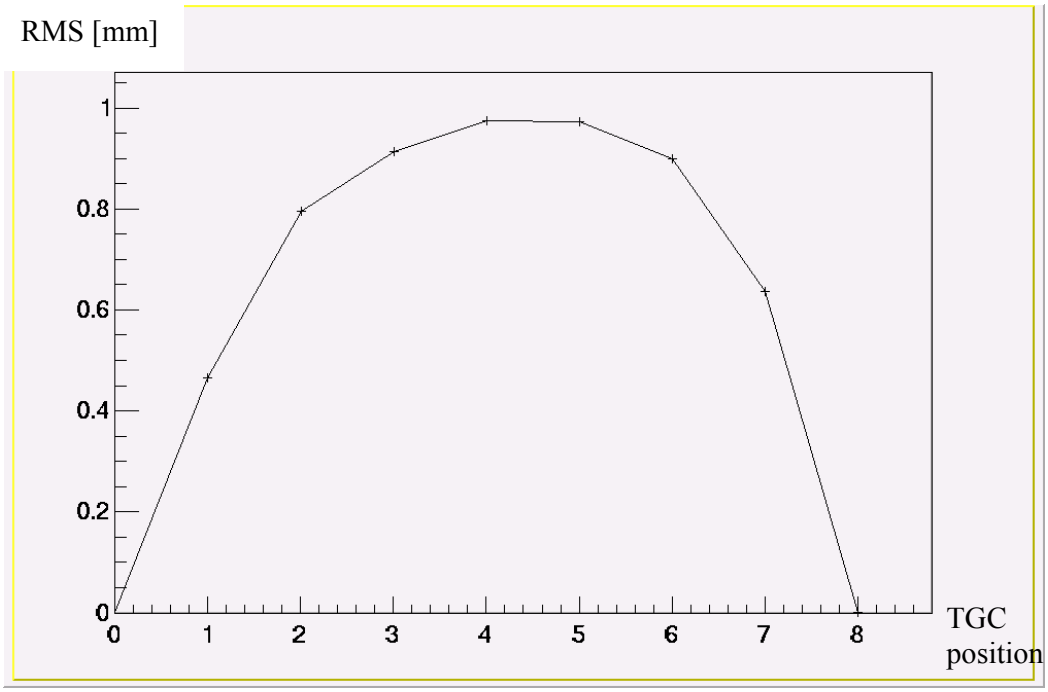

Fig 32: The graph of the widths in distributions in bottom plot of Fig. 31 as a function of the relative position in the testbench.

As expected the width of the errors calculated are larger in the center of the testbench (TGC 4) where the closer the chamber is to one of the PRCs the smaller is the effect of multiple scattering.

The combined PRC position measurement error and the multiple scattering uncertainties yield a total position uncertainty of less than five mm. This error is well below the efficiency histogram resolution.

7. Results

7.1. Efficiency mapping of tested chambers

In the following we use one of the chambers tested in the LAB, unit U08F2I-521.0, to demonstrate the operation of the testbench and to present the analysis program performance. The result of our quality control test is a mapping plot of the tested chamber efficiencies. This plot is produced by the offline analysis program in the following way:

- Two histograms are generated by the offline program. One is the position of muon crossing the TGC as extrapolated from the PRC coordinates (*Fig 33*). The second one presents hits that physically generated signals in the TDC unit, in both layers wires and strips (*Fig. 34*).
- The efficiency histogram is a result of a division of the histogram in *Fig. 34* by the histogram in *Fig 33*.
- The efficiency map is used for determination of the chamber global efficiency. The program checks each bin and count the number of bins with efficiency higher than 95% and 90% respectively.
- For estimating the total efficiency of the chamber it is compared to a reference ideal chamber histogram.

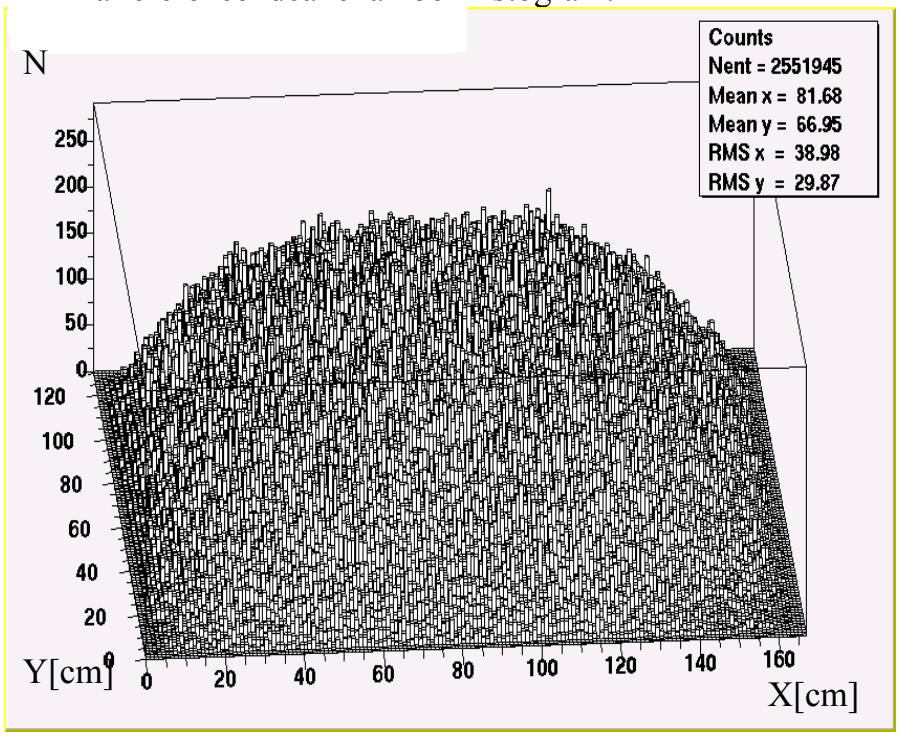

Fig 33: The hits expected in the TGC as extrapolated from the PRC information.

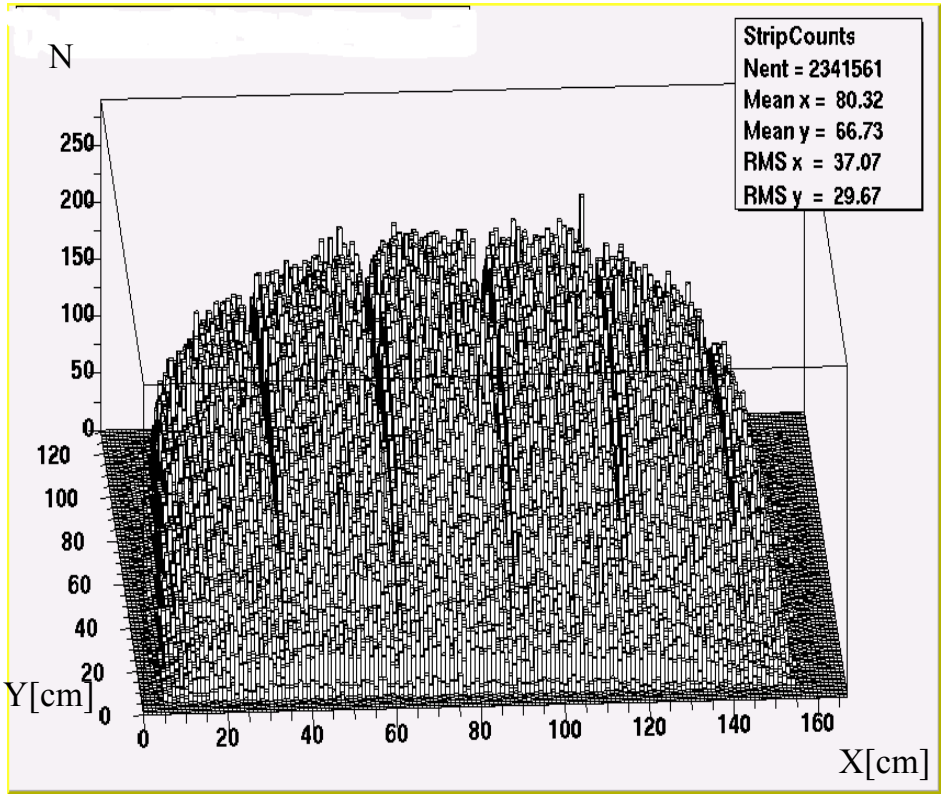

Fig. 34: The actual muons hits in the TGC.

The mapping plot contains the efficiency calculated separately for the wires and strips in every chamber. Therefore for a doublet we produce 4 plots two of strips and two of wires. The efficiency map of unit U08F2I-521.0 is shown in *Fig. 35* and
Table 3 which quantify the efficiency calculated for this unit.

Unit	**U08F2I-521.0**			
Layer	Detector 1 Wires	Detector 1 strips	Detector 2 wires	Detector 2 strips
	Percent of surface			
90% eff.	96.3%	97.0%	94.8%	94.8%
95% eff.	89.7%	90.9%	86.2%	86.4%

Table 3: Calculated efficiency of unit U08F2I-521.0

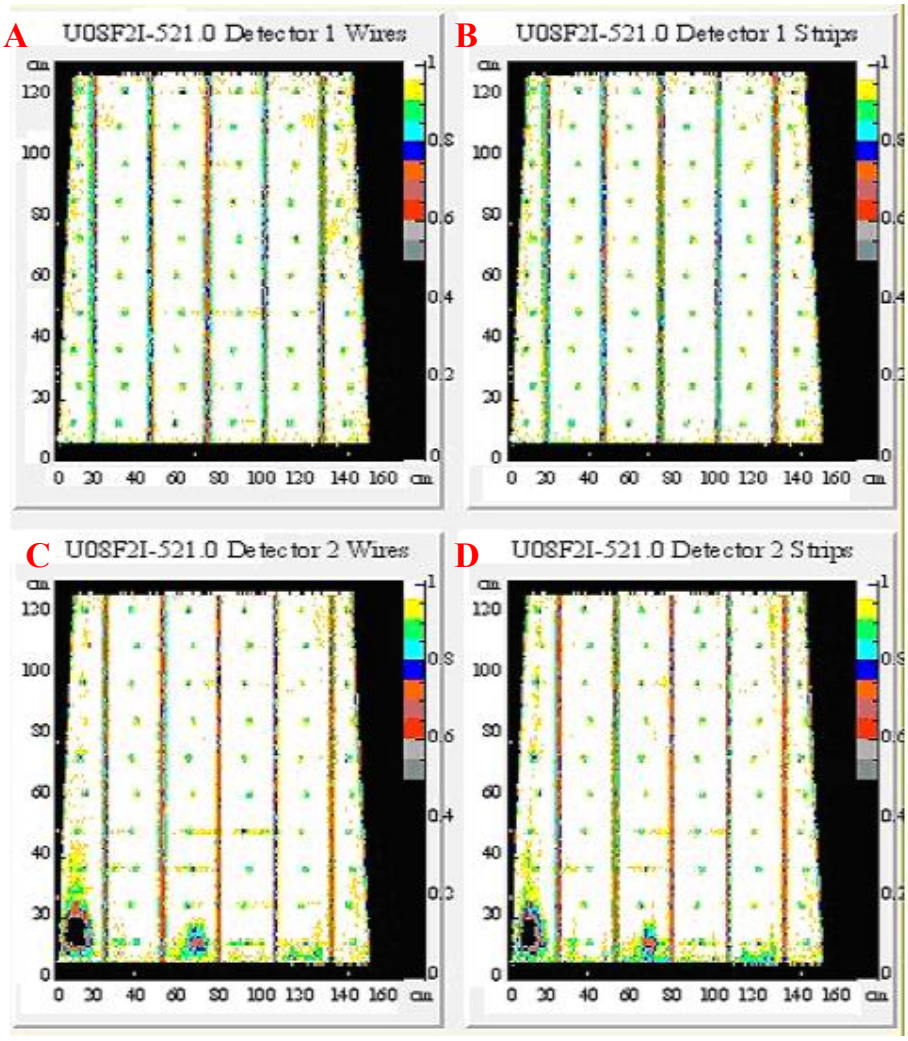

Fig. 35: The efficiency map of a doublet U08F2I-521.0. Figures A, B presents the wires (left) and Strips (right) of the bottom chamber, where C, D respectively present the wires and the strips of the top chamber. The colors stand for the efficiency in the measured surfaces. Efficiency >95% is white, 90-95% is yellow, 85-90% is green, where at the other side of the scale efficiency below50% is plotted in black.

As can be seen the chamber shown in the figure is not an ideal chamber. Nevertheless, the shape of tested TGC chamber is clearly seen and so is its internal structure. The inefficient lines parallel to the y axis, as well as the series of inefficient dots between them are well seen. These are the supports and support buttons positioned inside each chamber. Obviously they represent inactive areas as clearly seen in the efficiency plots.

One can see that the bottom chamber (figures A and B) efficiency is uniform on its entire surface where the top chamber (figures C, D) has

several inefficient areas. These inefficient regions may be a result of gluing problems during the construction of the chamber. The correlation between the strips and the wires inefficient regions tell us that these problems are due to the structure of the chamber itself and not electronics readout problems. The edges of the TGCs are sharp and there are no hits outside the chamber frame. It confirms that the entire surface is well covered by the PRC and the Scintillators, while the offline code correctly determines the trajectory and the hit points in the TGC.

In order to obtain a meaningful efficiency map, a cosmic muon sample of about ten million events is used. In the middle of the efficiency histogram each bin (1x1cm^2) contains about 250 hits going down to about 50 hits near the edges. This results in precision of about 1% in the centre and about 3% in the edges where the errors are calculated in the following way:

Eq. 5

$$\Delta\varepsilon = \sqrt{\frac{\varepsilon(1-\varepsilon)}{N}};$$

Here ε and $\Delta\varepsilon$ are the efficiency in a single bin and its error and N is the number of hits in that bin.

7.2. Alignment procedure

The procedure described above may introduce a bias to the measurement as a result of the way we align the chamber with respect to our coordinate system. In the following we describe a method developed in order to avoid such an uncertainty.
To demonstrate the problem we first plot a projection of the hits next to one of the support lines on the x axis. This projection plot is show in *Fig.36*.

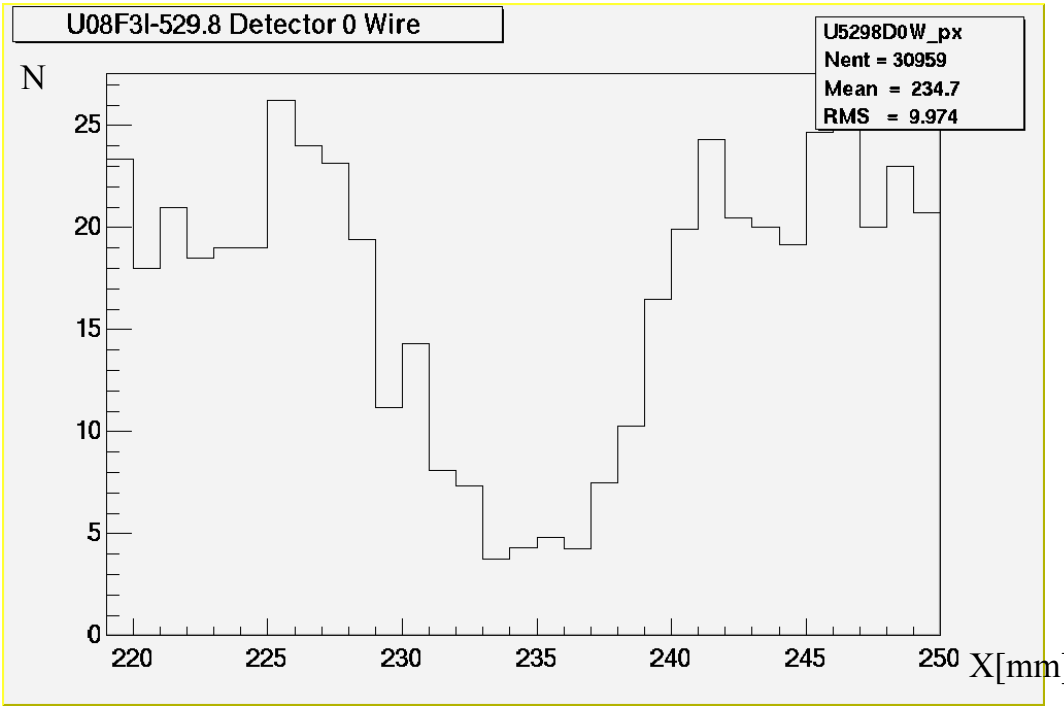

Fig.36: The profile of the single support in a resolution of one mm.

We know that the support width is 7 mm in the x direction. However due to electric field near the support and the resolution of our measurement the width of the inefficient region in the plot is slightly larger. Using bin size of 1 cm, a support can be either contained in one bin or occupy two bins. In case the support is spread between two bins the calculated active area will be lower than the theoretical expectation. This is enhanced by the fact the supports are approximately parallel to our y axis; hence all the bins along one support may behave in the same way. Moreover it is further enhanced if for a given chamber a few (or all) its supports suffer from the same misalignment, resulting in all of them being spread between two lines of bins. As a result we have a large uncertainty in the calculated efficiency resulting only from the positioning of the chamber in the reference coordinate system. To demonstrate the effect we plot *Fig. 37* . In that figure the chambers alignment was not tuned. Thus the typical widths of all the supports are wider than one bin size. The percentages of area with efficiency above 95% and between 90% to 95% are given in *Tab. 4*.

more than 95%	90% to 95%
94.18	2.76

Tab. 4: The efficiencies of the of the unaligned histogram in the example

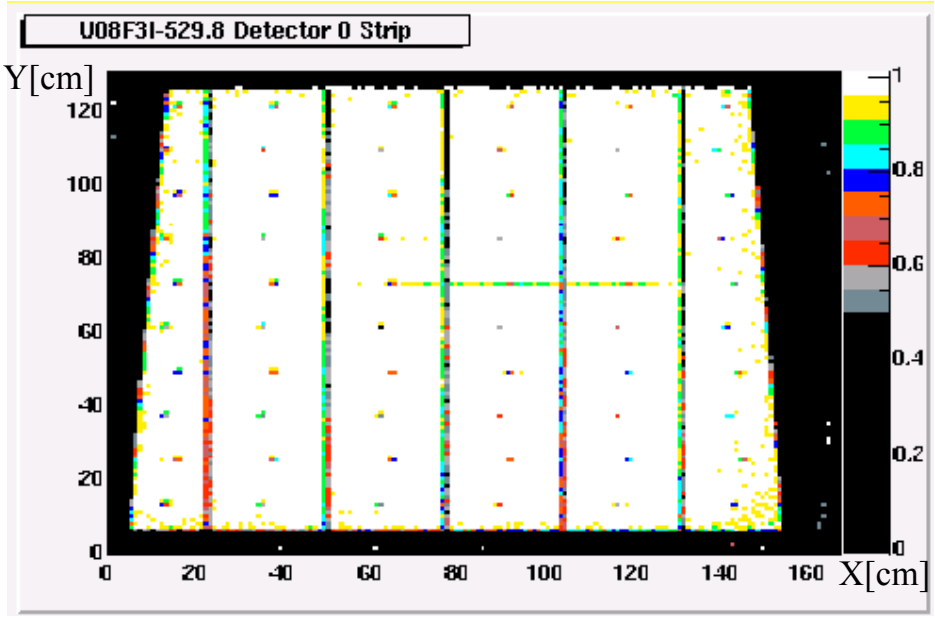

Fig. 37: An example of the unaligned chamber (strips) efficiency plot.

In order to minimize the inefficient area resulting from the positioning of the chambers with respect to the coordinate system, the following procedure is applied:

- A unit is analyzed by the offline program. Efficiency histograms, with bin size of 1x1 mm^2 are calculated. These histograms are depicted in the *Fig. 38.*

- The program finds all the points of the first left support. This is calculated by detection of the first left contiguous line of minimum points.

- It fits the detected points to a line and calculates the translation and rotation required in order to place this fitted line in the middle of a bin. In that way we minimize the artificial inefficiency resulting from the bins position.

- The analysis is repeated and the efficiency histograms with a bin size of one cm^2 are reproduced.

- The levels of efficiency corresponding to these histograms are calculated.

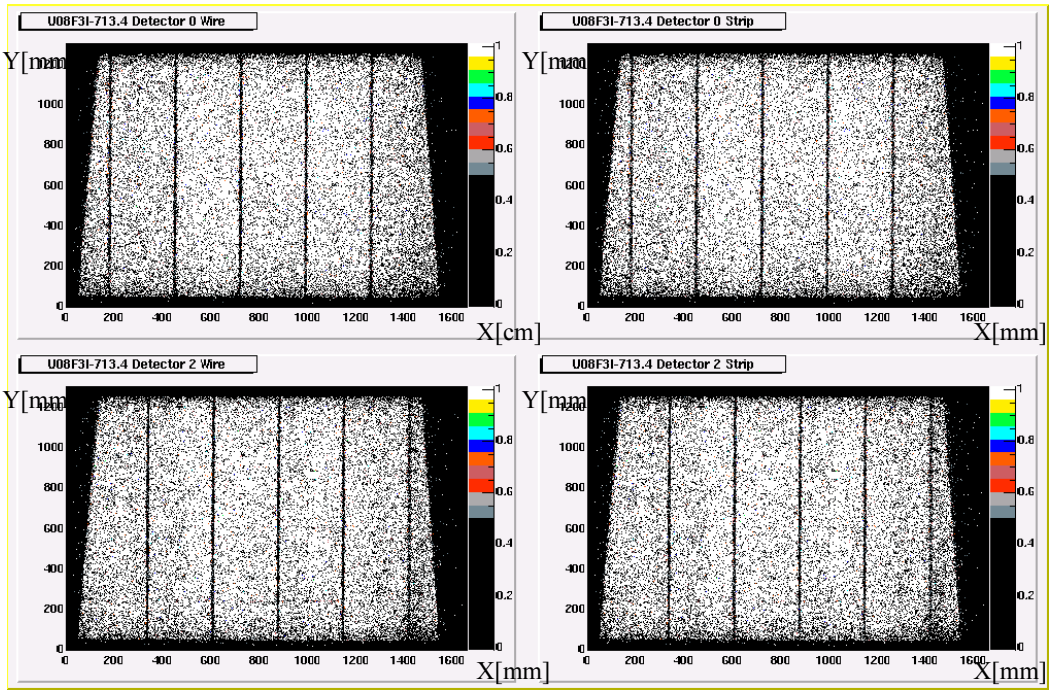

Fig. 38: The efficiency histograms (wires and strips of its two chambers) of the unit U08F3I-713.4, with bin size of one mm²

After tuning the alignment of this measured chamber the level of efficiency of those histograms is increased by about three percent. The corresponding modified numbers are shown in *Table 5*.

more than 95%	90% to 95%
96.13 (94.18)	3.7 (2.76)

Table 5 : The efficiencies of the of the aligned histograms in the example (in brackets the calculated efficiencies before the alignment procedure)

Fig. 39 shows the same efficiency plot of the chamber plotted in *Fig.36*, here after the alignment procedure applied.

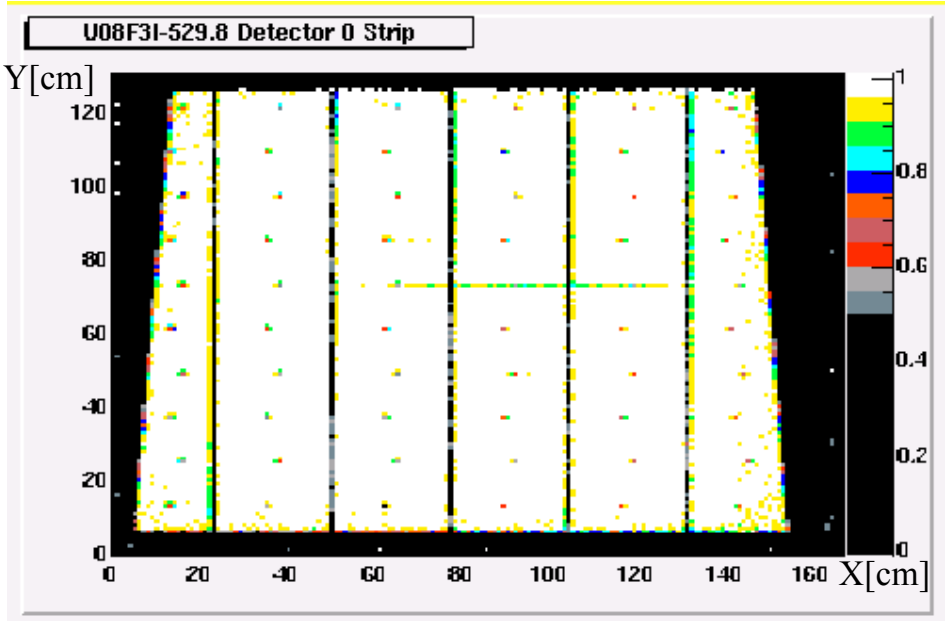

Fig. 39: The efficiency histogram of the chamber in Fig 36 here after the alignment procedure

This exercise has demonstrated that naively calculating the efficiency of a chamber may suffer from large uncertainties at the level of a few percents just from the geometrical positioning of the chamber in the coordinate system. However the above procedure can compensate for this additional uncertainty

7.3. Determination of the inefficient areas

As a criterion for the quality of a chamber it was decided to set a limit on the total area of inefficient regions. Inefficient area is defined as a contiguous area of more than 25 cm^2 that extends by more than 5 cm in each direction (x & y), with every point in that area having an efficiency of less than 95%.
The quality criterion is based on percentage of the integrated size of surface of all the inefficient areas in the detector. The integrated inefficient area should not exceed **5%** of the total active area of the detector. The calculation of the inefficient area is done including all the known supports lines and buttons.
The algorithm that calculates the integrated inefficient area is the following:

- Search for all the inefficient regions. By searching for 5x5 elements this search is not sensitive to the support lines and the buttons.
- Calculate the total area covered by these inefficient regions.

The technique is illustrated in *Fig. 40*. The top histogram shows the efficiency map of one chamber in a granularity of 1x1 cm^2. The second histogram shows the same chamber after the search for inefficient regions is applied. Here one can not see the supports seen in the top plot where the inefficient regions in the left low corner are well seen. Small inefficient regions and edges effects are naturally ignored.

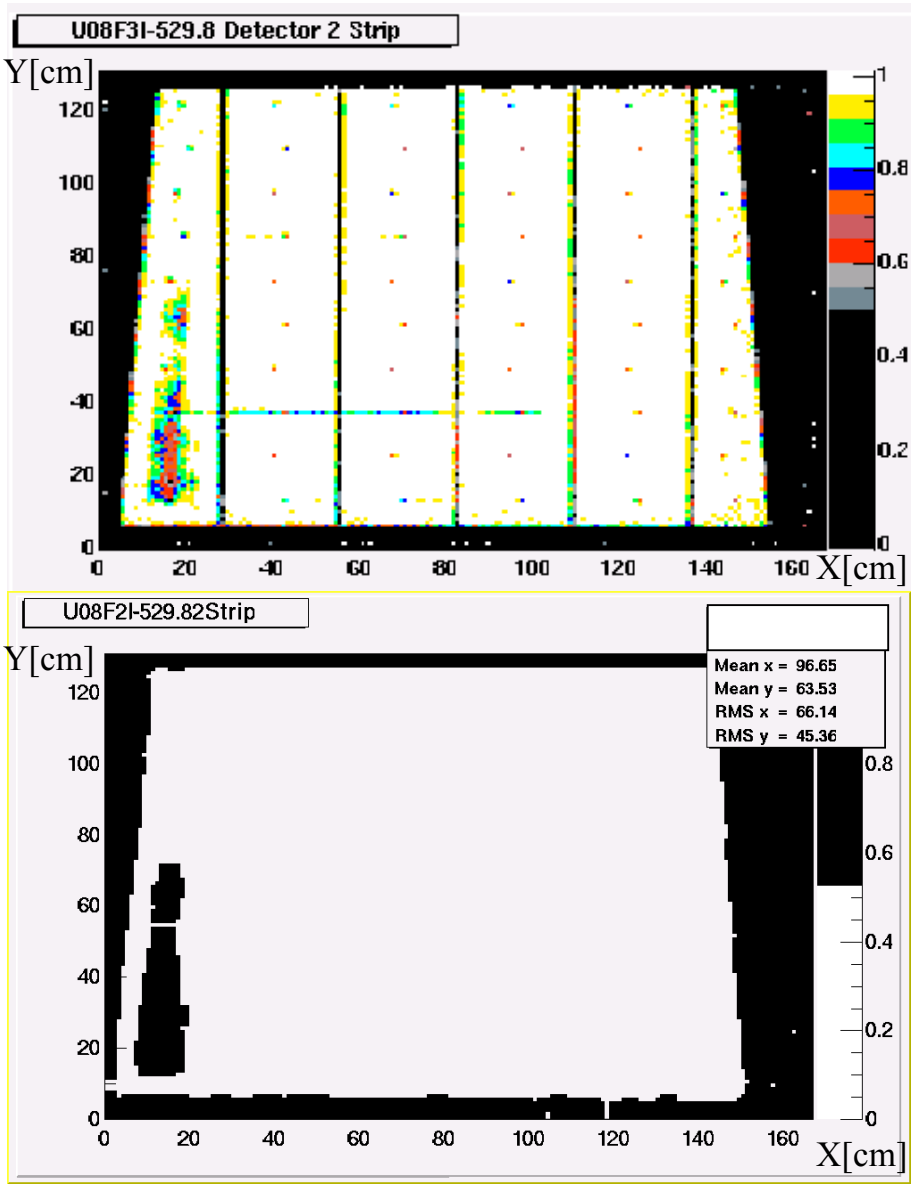

Fig. 40: Top – efficiency plot of one chamber's strip; Bottom - the detected inefficient regions in the above chamber.

In this example the total inefficient area was found to be 2.95% of the chamber total active area (supports included).

7.4. Potential problems

Several chambers defects can be detected in the testbench. Some of them are the pure hardware problems, and others are software related.

An example of a hardware fault which can be detected and sometimes fixed in our laboratory is demonstrated in the *Fig. 41*.

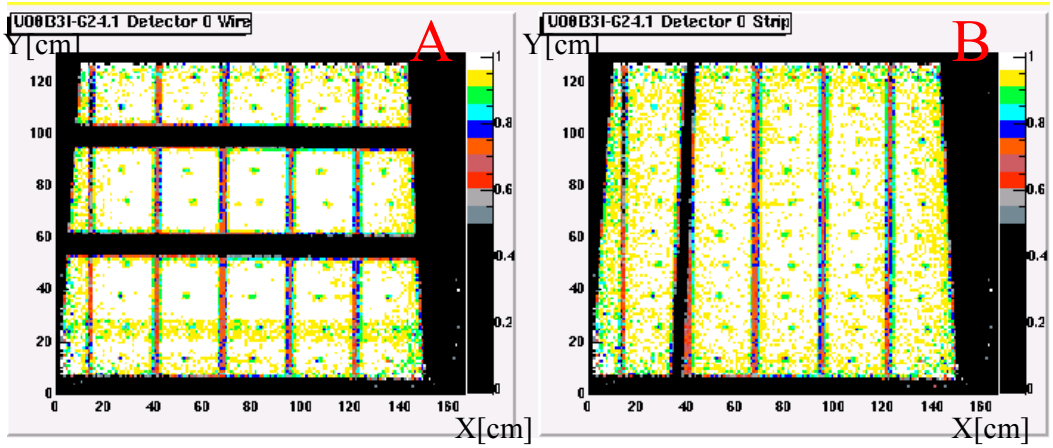

Fig. 41: The example of the unit U08B3I-624.1 with some imperfections

Two hardware defects that can be seen in this plot:

- One is inactive regions along the wires axis as shown *Fig. 41* A. This problem can occur due to the following faults:

    1. The ASD card, plugged on the chamber, is malfunctioning or bad connected.
    2. Faulty ASDreadout card.
    3. The signal cable from the ASD to the ASDreadout card is damaged.
    4. Wire groups in the chamber are disconnected.

- Second problem is missing strips as shown in *Fig. 41* B. This can also reflects problems in the ASD, ASDreadout, signal cable or disconnected strip.

These problems are treated in the following scheme:

1. Switch the signal cable from the ASD to the ASDreadout card; locate a problem either in the cable or in the readout electronics.

2. Replace the ASD card.
3. Record all the attempts to recover the problem and send the unit back to the manufacturing site.

7.5. High voltage dependence

The gain of multiwire chamber working in the saturated mode is strongly related to its operational voltage. The efficiency map of one TGC detector (wires on the left and strips on the right) shown in the *Fig. 42* . This plot is calculated when the chamber operates with the nominal high voltage of 2.9 kV.

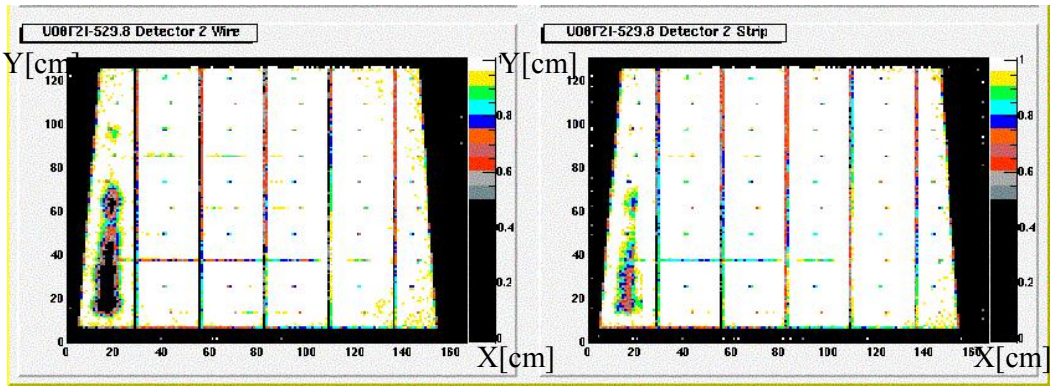

Fig. 42: The efficiency map of the one chamber operating at the nominal high voltage of the 2.9 kV.

There are inefficient areas on the left side of these two plots. Increasing the supplied high voltage to 3kV (*Fig. 43*), reduced the inefficient detected regions in this chamber.

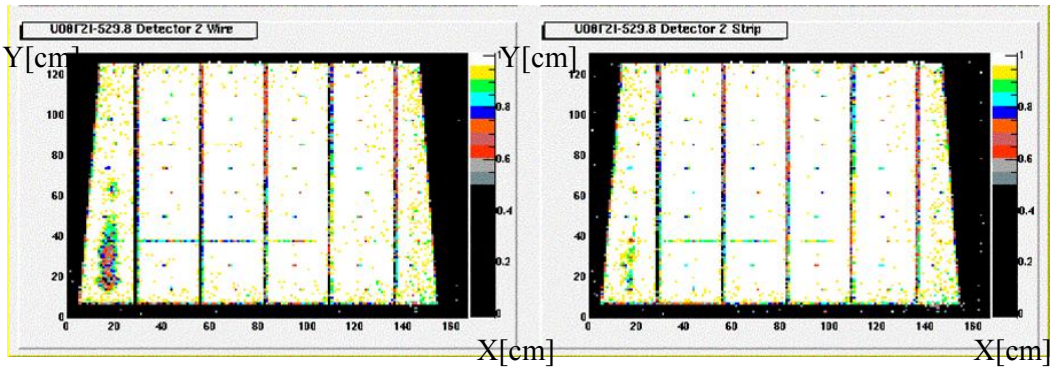

Fig. 43: The efficiency map of the same chamber (Fig. 42) operating at 3kV.

The results of TGC chambers tested operating in high radiation environment show some instabilities [8]. This has suggested setting the TGC nominal operating voltage to 2.9 kV. However, as shown above in some cases it is required to run the chamber in higher voltage up to 3kV. In the tests we run all the chambers at 2.9 KV. When needed we increase to 3 KV in steps of 50 volts, and record the changes in the results database.

8. Summary

This thesis describes the operation and results analysis of the muon cosmic ray telescope built in Tel-Aviv, in order to test the ATLAS muon endcap trigger chambers.

While still working on some improvements in the electronics equipment, time response measurements, and process automation the testbench recently went to a production mode. The testbench currently measures about 5 units per week. By now 46 TGC units were tested; forty one doublets and five triplets. Among the tested units two doublet units were produced in China and the rest at Weizmann Institute. One of the tested chambers could not hold HV; two of them had disconnected strips. These chambers were returned to manufacturing site for repair. All the results of the tests containing a detailed efficiency mapping and inefficient areas of each chamber are stored in a dynamic database to be further used in the ATLAS operation and analysis[9]. A distribution of tested chambers inefficient regions as calculated in section 7.3 is presented in *Fig. 44*.

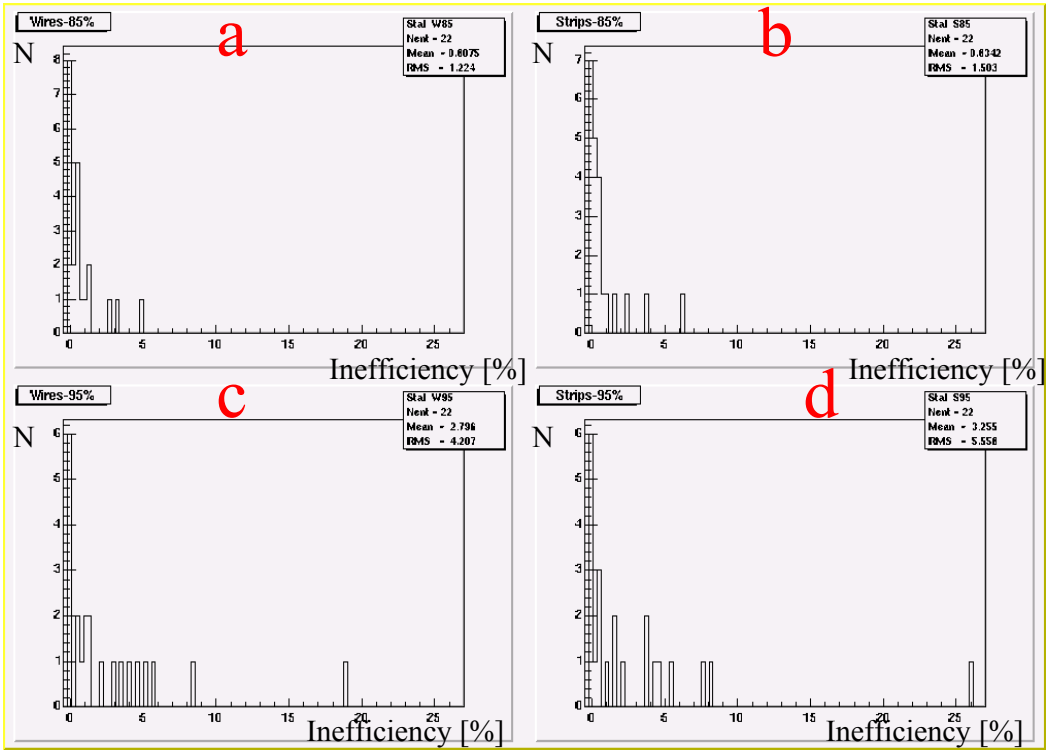

Fig. 44: Inefficient regions distribution, as detailed in the text.

Plot a (c) shows the wires readout distribution of regions with efficiency below 85% (95%), and plot b (d) describes similar distribution for the strips. Only one chamber in this plot has integrated inefficient region with efficiency below 85% at a level of 6-7% of its active area. When looking at the distribution of efficiencies above 95%, more than 18% of the area of this chamber does not pass this criterion. In three other chambers 6-8% of their area has efficiency below 95%. In the other chambers less than 5% of their area is less efficient than 95%.
The testbench is scheduled to run and check about 1000 TGC chambers in the next two-three years.

Appendix

Appendix I: **Binary online output file**

The offline program to calculate the TGC efficiency uses the information stored in the binary online output file. The online program writes the following details:

- TGC signal timing information - in order to evaluate their response time;
- HV information - in order to monitor the condition of high voltage;
- ADC (C-RAMS) information - in order to calculate the position of the muons when crossing the tested TGCs.

All the entries of that file are structured in four bytes long. Before each block of the data there is a pointer, which indicates the number of event, the type of the data and number of the 4 bytes words. There are two types of pointers:

- The pedestal data block;
- The TDC event data block.

In the following the structure of the output file:
One word (usually four bytes) is represented by:
FF FF FF FF in the hexadecimal base.

The pedestals[1] information is written as:
FF FF FF FF nn nn nn nn mm mm mm mm xx xx xx xx .. ..
where:
FF FF FF FF –is the pointer that indicates the beginning of the pedestals data block.
nn nn nn nn – is the number of pedestal words of ADC in channel1[2];
mm mm mm mm – is the number of pedestal words of ADC in channel0;
xx xx xx xx –is the pedestals data. It has structure of ADC output buffer.

The following presents the structure of the TDC event information block:
zz zz zz zz vv vv vv vv FF FF FC 19 kk kk kk kk yy yy yy yy .. ..
where:
zz zz zz zz –is the number of current event, starting at zero;
vv vv vv vv –is the number of the TDC data words;

[1] The pedestal is the data of ADC channels that include noise and signals.
[2] The channel1 and channel0 are representing the serial information from the upper and the lower precision chambers.

kk kk kk kk – is the HV status word. Each of the bits represents a status of one HV unit channel,
0 – means the channel is in normal mode, 1 – means the channel is in a trip mode;
yy yy yy yy – is the TDC event data. It has structure of TDC output buffer, including header and EOB (end of buffer).
The following explains the structure of the ADC (C-RAM) event:
zz zz zz zz hh hh hh hh pp pp pp pp oo oo oo oo .. ..
where:
zz zz zz zz – is the number of the current event;
hh hh hh hh – is the number of the ADC(C-RAMS) channel0 data words;
pp pp pp pp – is the number of the ADC(C-RAMS) channel1 data words;
oo oo oo oo –is the ADC(C-RAMS) event data. It has structure of the ADC (C-RAMS) output buffer.

```
00000000: FF FF FF FF 00 00 00 00|00 00 00 00 00 00 00 00
00000010: 00 00 00 04 FF FF FC 19|00 00 FF FF 00 40 00 00
00000020: 23 0B 2A 1B 00 20 00 00|00 00 00 00 00 00 00 06
00000030: 00 00 00 06 00 03 10 2E|00 03 20 31 00 2C 10 13
00000040: 00 2C 20 3D 00 2C 30 41|00 2C 40 16 00 03 D0 65
00000050: 00 03 E0 51 00 27 00 2B|00 27 10 63 00 27 20 4C
00000060: 00 27 30 23 00 00 00 01|00 00 00 03 FF FF FC 19
00000070: 00 00 FF FF 00 40 00 00|00 20 00 00 00 00 00 01
00000080: 00 00 00 06 00 00 00 0C|00 09 A0 12 00 09 B0 34
00000090: 00 09 C0 2D 00 23 40 1C|00 23 50 48 00 23 60 3F
000000A0: 00 23 70 1B 00 2A 00 19|00 30 00 17 00 30 60 0E
000000B0: 00 32 A0 12 00 32 F0 1D|00 00 00 72 00 0B B0 26
000000C0: 00 0B C0 21 00 1F 30 2A|00 1F 40 33 00 1F 50 1D
000000D0: 00 00 00 02 00 00 00 03|FF FF FC 19 00 00 FF FF
000000E0: 00 40 00 00 00 20 00 00|00 00 00 02 00 00 00 00
000000F0: 00 00 00 08 00 10 D0 1B|00 11 50 2A 00 11 60 6D
00000100: 00 11 70 31 00 32 D0 2E|00 32 E0 8B 00 32 F0 7D
00000110: 00 33 00 1C 00 00 00 03|00 00 00 03 FF FF FC 19
```

Fig. 45: Shows a typical output file.

Offset	Value	Description
0x000	0xFF FF FF FF	Start of pedestal block
0x004	0x00 00 00 00	Number of words of the ADC channel0
0x008	0x00 00 00 00	Number of words of the ADC channel1.
0x00C	0x00 00 00 00	Number of the event.
0x010	0x00 00 00 04	Number of the TDC event data.
0x014	0xFF FF FC 19	Start of the TDC event block.
0x018	0x00 00 FF	HV status, dummy value.

	FF	
0x01C	0x00 40 00 00	Header of the TDC event.
0x020	0x23 0B 2A 1B	The TDC event data.
0x024	0x00 20 00 00	Eob of the TDC event
0x028	0x00 00 00 00	Number of the event.
0x02C	0x00 00 00 06	Number of words of the ADC channel0 data.
0x030	0x00 00 00 06	Number of words of the ADC channel1 data.
0x034 – 0x048	0xnn nn nn nn	The ADC channel1 data.
0x04C – 0x064	0xnn nn nn nn	The ADC channel0 data.
0x068	0x00 00 00 01	Number of the event.

Table 6: The binary online output file has the following structure.

A double line is marking one block of the event data.

Online Monitoring

During its execution the online program produces three output ASCII files. These files are used to monitor the system behaviour during a testing period. An analysis graphical program plots histograms out of the data from ASCII files. Thus the user can detect errors in the system during the testing period.
The files contain incremental data collected from the ADC and the TDC units.
One file contains the active PRC channels. In a typical event several channels (3-5 in each coordinate) sense the passage of a charged particle through that detector. Two arrays of the data (75 values each) are written to this file. They contain the data from ADC channel0 and channel1, respectively. The monitoring program counts the number of hits per channels. The second file contains the active channels ADC channel0 and channel1data. Two arrays of size of 864 (number of channels to be read by ADC) are written to that file. The monitoring program counts the number of hits in each channel. The third file contains the active channels in the TDC. An array of 128 values is written to that file, and the monitoring code counts the number of entries in each channel.

Appendix II: **The multiple scattering**

Many small-angle scatters deflect a charged particle traversing any medium. Most of these deflections are due to Coulomb scattering from nucleis. The Coulomb scattering distribution is well represented by the theory of Moliere[10]. It is roughly Gaussian for small deflection angles, but at larger angles (greater than a few θ_0, defined below) it behaves like Rutherford scattering, having larger tails than does a Gaussian distribution.
If we define:

$$\theta_0 = \theta_{plane}^{rms} = \frac{1}{\sqrt{2}}\theta_{space}^{rms}$$

Eq. 6

Then it is sufficient for many applications to use a Gaussian approximation for the central 98% of the projected angular distribution, with a width given by [11].

$$\theta_0 = \frac{13.6MeV}{\beta cp} z\sqrt{x/X_0}[1+0.038\ln(x/X_0)]$$

Eq. 7

Here p, βc, and z are the momentum, velocity, and charge number of the incident particle, and x/X_0 is the thickness of the scattering medium in radiation lengths.
This value of θ_0 is from a fit to Moliere distribution for singly charged particles with $\beta = 1$ for all Z, and is accurate to 11% or better for $10^{-3} < x/X_0 < 100$.
Eq. 7 describes the scattering from a single material, while the usual problem involves the multiple scattering of a particle traversing many different layers and mixtures. Since it is from a fit to a Moliere distribution, it is incorrect to add the individual θ_0 contributions in quadrature; the result is systematically too small. It is much more accurate to apply *Eq. 7* once, after finding x and X_0 for the combined scatterer.
When we substitute the Cosmic Rays and the TGCs nominal values to *Eq. 7* we evaluate the scattered angle to be about 0.23^o for each TGC

triplet unit.
Thus, the maximal effect of multiple scattering is expected to be less than 0.8 cm, which is less than the chosen efficiency histogram bin size ($1cm^2$) and therefore ignored.

Bibliography

[1] S. Glashow, Nucl. Phys. 22 (1961) 579;
S. Weinberg, Phys. Rev. Lett. **19** (1967) 1264;
A. Salam, "Elementary Particle Physics", W. Svartholm, ed., Almquist and Wikesel, Stockholm, 1968.

[2] P.W. Higgs, Phys. Rev. Lett. **12** (1964) 132 and Phys. Rev. **145** (1966) 1156 ; F. Englert and R. Brout, Phys. Rev. Lett. **13** (1964) 321.

[3] ATLAS TDR 15, CERN/LHCC/99-15, vol 2, page 673.

[4] E.Richter-Was et al., "Minimal Supersymmetric Standard Model Higgs rates and backgrounds in ATLAS", ATLAS Internal Note ATL-PHYS-96-074 (1996) , published in Int. J. Mod. Phys. A13 (1998) 1371

[5] ATLAS TDR 15, CERN/LHCC/99-15, vol 2, page 829.

[6] S. Dado et al., Nucl. Instrum. Methods **A252** (1986) 511;
G. Mikenberg, Nucl. Instrum. Methods **A265** (1988) 223.

[7] C. Beard et al., Nucl. Instrum. Methods **A286** (1990) 117.

[8] S. Majewski et al., Nucl. Instrum. Methods **217** (1983) 265;
G. Bella et al., Nucl. Instrum. Methods **A252** (1986) 503 .

[9] http://lep1.tau.ac.il/tgc/ - The dynamic database that stores the information of the test runs and the tested chambers in the Tel-Aviv cosmic rays testbench.

[10] H.A. Bethe, Phys. Rev. **89**, 1256 (1953).

[11] . V.L. Highland, Nucl. Instrum. Methods **129**, 497 (1975), and Nucl. Instrum. Methods **161**, 171 (1979).